Simulating inhomogeneous spacetimes using the ADM-formalism

Master's Thesis, 15.11.2021

Author:

Olli Väisänen

Supervisors:

Kimmo Kainulainen
Enrico Schiappacasse

UNIVERSITY OF JYVÄSKYLÄ
DEPARTMENT OF PHYSICS

Abstract

Väisänen, Olli Jaakko Rikhard
Simulating inhomogeneous spacetimes using the ADM-formalism
Master's thesis
Department of Physics, University of Jyväskylä, 2021, 99 pages.

There is an extensive literature on the effects of inhomogeneities on the expansion of the universe and measurable quantities. However, as there is no known general solution to Einstein's field equations, much of the analysis relies on perturbation theory and very symmetric toy models. In this thesis, I will assess a method of studying the effects of inhomogeneities using fully relativistic simulations. To this end, I will introduce the Arnowitt-Deser-Misner- and Baumgarte-Shapiro-Shibata-Nakamura -formulations (ADM- and BSSN-formulations) for general relativity and discuss the numerical stability of the ADM-formalism with different initial conditions in a matter dominated universe. The stability of the results depends heavily on the chosen length scale. On very large scales (~ 500 Mpc) the results appear reliable until late in the evolution, whereas on more physically relevant scales (~ 100 Mpc) the equations are almost immediately unstable. Further research should move on to the more stable BSSN-formalism. In addition, I implemented a simulation for calculating observed redshifts in numerical spacetimes and assessed its results qualitatively. The preliminary results suggest an apparent deformation of density perturbations due to gravitational lensing.

Keywords: General relativity, Numerical relativity, ADM-formalism, Inhomogeneous cosmological models, Numerically simulated redshift

Tiivistelmä

Väisänen, Olli Jaakko Rikhard
Epähomogeenisten aika-avaruuksien simuloiminen ADM-formalismin avulla
Pro gradu -tutkielma
Fysiikan laitos, Jyväskylän yliopisto, 2021, 99 sivua

Maailmankaikkeuden epähomogeenisuuksien vaikutuksia sen laajenemiseen ja mittaustuloksiin on tutkittu kirjallisuudessa paljon. Koska Einsteinin yhtälöille ei tunneta yleisiä ratkaisuja, nämä tutkimukset ovat kuitenkin perustuneet häiriöteoriaan ja hyvin symmetrisiin, yksinkertaistettuihin malleihin. Tässä tutkielmassa selvitän, kuinka epähomogeenisuuksien vaikutuksia olisi mahdollista tutkia käyttämällä täysin relativistisia numeerisia simulaatioita. Tätä varten esittelen Arnowitt-Deser-Misner- ja Baumgarte-Shapiro-Shibata-Nakamura -formalismit (ADM- ja BSSN-formalismit) yleiselle suhteellisuusteorialle ja tutkin ADM-formalismin numeerista stabiiliutta erilaisilla alkuarvoilla aineen dominoimassa maailmankaikkeudessa. Saamieni tulosten stabiilius riippui vahvasti simulaatioille valitusta pituusskaalasta. Hyvin suurilla skaaloilla ($\sim$ 500 Mpc) tulokset olivat varsin luotettavia simulaation loppuhetkiä lukuun ottamatta, kun taas fysikaalisesti merkittävillä pituusskaaloilla ($\sim$ 100 Mpc) yhtälöt olivat lähes välittömästi epästabiilit. Jatkotutkimuksissa tulisi siirtyä ADM-formalismista luotettavampaan BSSN-formalismiin. Tämän lisäksi laadin simulaation havaittujen punasiirtymien laskemiseksi numeerisista aika-avaruuksista ja arvioin sen tuloksia kvalitatiivisesti. Alustavien tulosten mukaan näennäiset tiheysvaihtelut vääristyvät gravitaatiolinssi-ilmiön vuoksi.

Avainsanat: Yleinen suhteellisuusteoria, Numeerinen suhteellisuusteoria, ADM-formalismi, Epähomogeeniset kosmologiset mallit, Numeerisesti simuloitu punasiirtymä

Preface

I thank my supervisors Kimmo Kainulainen and Enrico Schiappacasse for patience and support in this long project. Also, my gratitude goes to my family for keeping me sane through the pandemic and to my friends for doing the opposite. This thesis would not exist without you.

Jyväskylä November 15, 2021

Olli Väisänen

Contents

1 Introduction

An observation at the heart of modern cosmology is the cosmological principle. The principle states that at large enough scales, typically taken to be approximately 300 Mpc, the universe is both homogeneous and isotropic[1] [1]. In truth, the principle is in part an assumption, as our observations are naturally limited to our own location on Earth, and there still exists some debate on whether the universe actually is homogeneous on the very largest scales [2, 3]. However, despite the limitations the cosmological models relying on the cosmological principle have been extremely successful.

The simplest of such models, the Friedmann-Lemaître-Robertson-Walker -universe (FLRW-universe), is found by applying Einstein's general relativity and our knowledge of the matter content of the universe on a homogeneous and isotropic spacetime [4]. The result is the familiar picture of an expanding universe with a hot and dense Big Bang at the beginning and an end state dependent on the matter composition [4].

Nevertheless, there are aspects of our observed universe which cannot be captured by such a simple model. In particular, from everyday experience we know that the universe contains inhomogeneities, such as galaxies, stars and humans, which cannot arise in the perfectly homogeneous FLRW-universe. A solution can be found by noting that since gravity tends to draw matter together, in the distant past these inhomogeneities must have been much smaller. Thus, if one assumes that on average the universe behaves as if it was homogeneous, it is possible to treat small inhomogeneities using linear perturbation theory [5, 6]. These small initial ripples, perhaps arising from the quantum fluctuations of the Big Bang, would then grow and eventually collapse into the gravitationally bound objects we observe today [6]. A model of this kind fits our observational data very well and forms the so-called standard model of cosmology, or ΛCDM [4].

However, the above description does contain assumptions that warrant a closer look. The one I will focus on in this text is whether the average behavior of the

---

[1] Homogeneous: The universe looks the same at every point. Isotropic: The universe looks the same in every direction.

universe matches the homogeneous case. Setting the question of the homogeneity of the very largest scales aside, the effects of the structure at and below the scale of 100 Mpc is not entirely clear either.

On a theoretical level, the origin of many of the issues is the nonlinear nature of the Einstein's field equations. As opposed to averaging a linear equation, taking the average of Einstein's equations will yield extra terms compared with the homogeneous case [7]. This effect is called cosmological backreaction, and there exists a considerable amount of literature on the subject. The reader may consult [8] for a review.

Another problem arises from the observations we use to test our models themselves. Apart from the recent observations of gravitational waves, all of our observations on the distant universe rely on received electromagnetic radiation. The problem with the measurements is that the way the quantities of interest are calculated from the measured data can in general depend on the inhomogeneities the radiation encounters on the way [8, 9].

An important example of this are the measurements of distance and redshift. Distances in cosmology are typically measured by comparing either the apparent luminosity or the angular size of an object to a theoretical prediction. As the curvature of the spacetime can affect the trajectories of light rays, inhomogeneities can act as a lens and modify the observed distances [9, 10]. The measured redshifts are changed in a similar way [9], and it is not clear whether or not these alterations average to zero over long distances.

A third issue is due to the increasing accuracy of the observations. Recent cosmological measurements, such as the Planck survey [11], provide tests to cosmological models with unprecedented accuracy, and even if the effects of inhomogeneities remain small, they can no longer be ruled out as sources of possible discrepancies with the data.

One particularly large such discrepancy is the so-called Hubble tension. The rate of the expansion of the universe, the Hubble constant, can be measured in several different ways. Some methods rely on measurements of the cosmic microwave background (CMB) [11] and consequently on information from the very early universe. In contrast, many other methods, such as those in [12], observe phenomena which occur at much later times. The early- and the late-time methods result in different Hubble rates, and the statistical significance of this discrepancy has only grown with more accurate measurements. Various different explanations have been proposed to the Hubble tension [13]. Some models explore the effects of inhomogeneities on the tension, although there is recent evidence against it as well [14]. No explanation is deemed conclusive at this moment.

These problems would naturally vanish if one could obtain an exact solution for the spacetime of the universe. As solutions to Einstein's field equations are only known for the most symmetric physical situations, until very recently the study of inhomogeneities has focused on very simplified toy models [15]. One well-studied class of models are the spherically symmetric Lemaitre-Tolman-Bondi -spacetimes (LTB-spacetimes) and the "Swiss cheese -models" derived from them [16]. The results obtained using models such as these often suggest that the effects of the inhomogeneities are small, but it is possible that this is only an artefact of the high degree of symmetry involved [15].

The situation is likely to change, as the numerical methods for solving Einstein's equations have seen remarkable development over the past couple decades. Numerical relativity itself is not a new field of study. For instance, one particularly influential formulation by Arnowitt, Deser and Misner dates back to 1959 (ADM-formalism) [17]. However, the early attempts at numerical relativity suffered from severe numerical instability which limited their applications to very symmetric spacetimes such as the ones mentioned above [18].

Many of the stability issues were only solved very recently. While there are many different modern formulations [18], the most commonly used one is the Baumgarte-Shapiro-Shibata-Nakamura -formalism (BSSN-formalism) developed two decades ago [19, 20]. The modern formulations have seen remarkable success in running previously unstable simulations, the most well known of which is the successful calculation of a gravitational wave waveform [21, 22]. In the past ten years, numerical relativity has also found its way to cosmology due to the availability of tools such as the Einstein toolkit [23–26].

In this thesis, I will explore how to simulate the large scale structure of the universe, such as galaxy filaments, using numerical relativity. The simulation will loosen the spherical symmetry of the simplest models. However, to manage the computational time, I will consider two models with cubic lattice symmetry and assume that the universe is filled with pressureless dust. In order to limit the scope of the thesis, I will only implement the ADM-solver for the Einstein equations. For future use I will still detail the theory behind the BSSN-formulation and address whether it is necessary for performing the calculation accurately. Lastly, I will implement a numerical simulation for calculating the trajectories of light rays and the associated redshifts in an inhomogeneous spacetime.

I will begin by briefly describing some basic results necessary for later development in chapter 2. After this, I will detail the ADM- and BSSN-formulations of Einstein's field equations and their respective initial conditions in chapters 3 through 5. In the last theoretical chapter, I will discuss light propagation in a curved spacetime. Afterwards in chapter 7, I will go through the numerical methods necessary in implementing the ADM-equations. To end the thesis, I will give some preliminary results of the ADM-simulations and discuss them more closely in chapters 8 and 9.

1.1 Notation and conventions

This text will largely use the notation and conventions in [18]. I will use the signature $(- + ++)$ for the metric throughout the text and always set the speed of light and the gravitational constant $c = G = 1$ unless specified otherwise. Greek letter indices are assumed to run over all four coordinates, while Latin indices run over only the spatial ones. Symmetric and antisymmetric parts of a tensor are defined in the usual way,

$$T_{(ab)} = \frac{1}{2}(T_{ab} + T_{ba}) \tag{1}$$

and

$$T_{[ab]} = \frac{1}{2}(T_{ab} - T_{ba}), \tag{2}$$

with the obvious generalization to more indices. Covariant derivatives will be denoted by ∇, and the derivatives will always be taken with respect to the Levi-Civita connection defined below in section 2.

2 Basic results in cosmology

In order to begin, I need to introduce some results that will turn out to be useful later on. Both here and later on in this text, I will assume that the reader is familiar with the basic concepts of differential geometry, tensor calculus and general relativity. For a more complete treatment on the mathematics involved the reader may consult for example [27, 28], and I will only skim through the details on these subjects. I will start this section by giving a short overview on what our current understanding on large-scale structure of the observed universe is and how it has developed. After this, I will introduce the FLRW-model for a homogeneous and isotropic universe and briefly touch on how to treat small perturbations on the FLRW-background.

2.1 The large-scale structure of the observed universe

The first indications of structure beyond our own Milky Way were the observations of nebulae, and there was speculation that they were similar in nature to the Milky Way already in the 18th century [29]. Actual rigorous evidence of this had to wait for improvements in technology. Early 20th century measurements of the redshifts of nebulae revealed that their velocities were far larger than those of stars in the Milky way and shortly thereafter the best telescopes could resolve the spiral structure of some nebulae [29]. The matter was largely settled by 1929, when Edwin Hubble published a paper on resolving Cepheid variable stars in the Andromeda galaxy, which could be used in more accurate measurements of distance [30].

The theory of the evolution of the universe got its start roughly in parallel with these developments. One key advance that marked the turn of the twentieth century was Einstein's general relativity, which was introduced in 1915. Shortly thereafter, general relativity was independently applied to a homogeneous universe by Friedmann and Lemaître [31, 32], and over time these models led to the current Friedmann-Lemaître-Robertson-Walker -models [33–36]. These models introduced the idea of an expanding universe, which was soon confirmed by Hubble's observations in 1929 [37].

The development since has been rapid. A landmark discovery was the accidental measurement of the cosmic microwave background by Wilson and Penzias in 1965 [38]. This cemented the consensus around the hot Big Bang-models of the early universe. On another note, the presence of dark matter was discovered both in the rotation curves of individual galaxies and in the large-scale behaviour of galaxy clusters in various studies in the first half of the twentieth century [39, 40]. By the end of 1980s, dark matter was understood to form the skeleton structure around which luminous matter coalesces [41].

For the majority of the twentieth century, the large-scale structure of the universe was thought to consist of galaxy groups and galaxy clusters, ranging in scale up to 5 Mpc. However, starting from the 1980s, galaxy surveys have found even structures, such as galaxy filaments and voids. (See [42, 43] for examples.) This development has continued all the way up to present day, which has raised some questions about the validity of the cosmological principle.

By the turn of the twenty-first century, cosmology had largely entered its current era with the discovery of the dark energy [44, 45] and the various microphysical processes underlying the evolution of the early universe [4]. As I mentioned in the introduction, precision measurements have shifted the focus in cosmology to small deviations from the standard models.

I will now give a short summary of the structure of the universe according to the our current knowledge. The energy density of our universe consists of approximately 63.8% dark energy, 26.5% dark matter and 4.9% ordinary baryonic matter [11]. On the smallest length scales, ordinary matter has collapsed into planets, stars and galaxies, and on these scales dark matter forms a massive but dilute halo around each galaxy. Galaxies in turn form groups and clusters, which again group into larger structures. In the end, these clusters lie in massive string-like structures called galaxy filaments, whose mass consists mainly of dark matter. The filaments are embedded into nearly empty void and together they form the aforementioned cosmic web [4]. Figure 1 depicts a portion of simulated cosmic web from the Millenium simulation [46]. Beyond the scale of the cosmic web, at scales upwards from 300 Mpc, the universe is usually deemed to become homogeneous [1].

According to the best models of today, the evolution of this structure began with small perturbations in energy density, which arose as a result of inflation or some other process during a hot Big Bang. The energy density of very early universe was dominated by relativistic particles, or radiation. The current particle composition

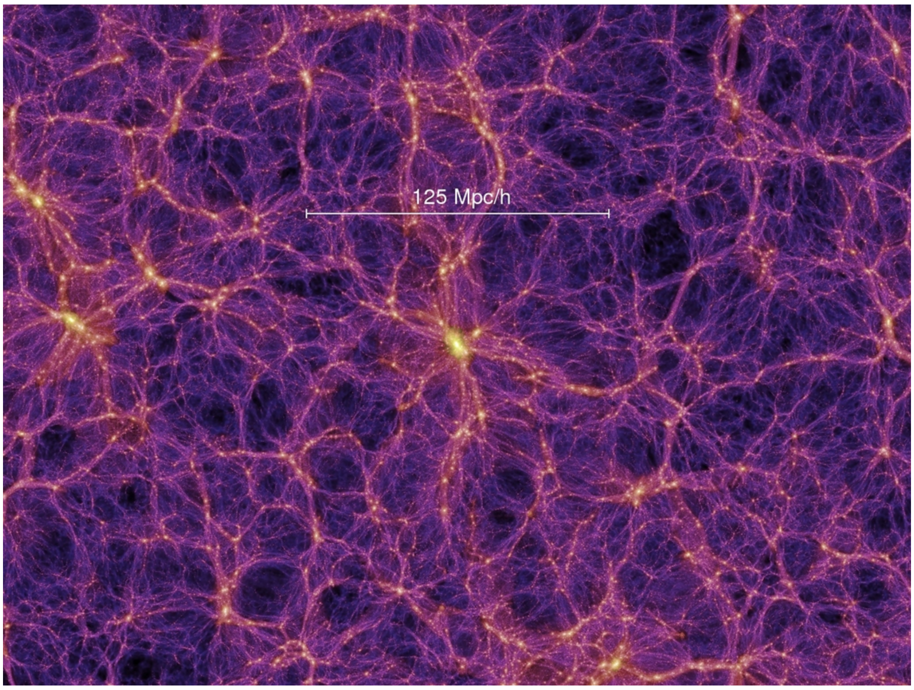

Figure 1. A simulated portion of the cosmic web produced by the Millenium Simulation [46]. Image retrieved from `https://wwwmpa.mpa-garching.mpg.de/galform/virgo/millennium/`.

was created in various processes during the early radiation-dominated era, but the density perturbations did not yet start growing [41]. As the universe cooled down non-relativistic matter eventually became the dominant component of energy density. The cosmic microwave background formed approximately 380 000 years after the Big Bang or equivalently at redshift[2] $z \approx 1100$, when electrons and protons combined to form atoms and the universe became electrically neutral. This allowed radiation to propagate unimpeded, and thus the CMB is the earliest electromagnetic signal measurable. [4]

The existing density perturbations began growing due to their gravitational pull at the onset of the matter-dominated era [41]. Over time the baryonic matter would coalesce at the same structure due to the gravitational attraction of the dark matter. Eventually the density perturbations grew enough to enter the nonlinear regime and collapsed forming the largest gravitationally bound objects such as galaxy clusters, though the specifics of the collapse depend on the models used [41]. The collapse would occur on smaller scales as well forming galaxies and the first stars. This process as a whole is known as the structure formation. Currently the energy density

---

[2] See chapter 6 for more information on redshift.

of the universe is dominated by dark energy [4].

2.2 The Friedmann-Lemaître-Robertson-Walker -universe

The behavior of the universe as a whole is determined by general relativity accompanied with the microphysics that determine the equation of state for the matter. While there is extensive literature on the subject, I will only give the most relevant results. A more complete treatment can be found in [27].

The curvature of a manifold such as the spacetime is determined by the metric $g_{\mu\nu}$ specifying the length element

$$ds^2 = g_{\mu\nu} dx^\mu dx^\nu. \tag{3}$$

More specifically, the curvature is expressed with the Christoffel symbols associated with the metric,

$$\Gamma^\mu_{\alpha\beta} = \frac{1}{2} g^{\mu\nu} (\partial_\alpha g_{\nu\beta} + \partial_\beta g_{\nu\alpha} - \partial_\nu g_{\alpha\beta}), \tag{4}$$

and the Riemann tensor

$$R^\mu{}_{\nu\alpha\beta} = \partial_\alpha \Gamma^\mu_{\beta\nu} - \partial_\beta \Gamma^\mu_{\alpha\nu} + \Gamma^\mu_{\alpha\lambda} \Gamma^\lambda_{\beta\nu} - \Gamma^\mu_{\beta\lambda} \Gamma^\lambda_{\alpha\nu} \tag{5}$$

constructed using them [27]. The contractions of the Riemann tensor, namely the Ricci tensor $R_{\mu\nu} = R^\alpha{}_{\mu\alpha\nu}$ and the Ricci scalar $R = g^{\mu\nu} R_{\mu\nu}$, are further used to define the Einstein tensor $G_{\mu\nu} = R_{\mu\nu} - \frac{1}{2} g_{\mu\nu} R$. These objects have a variety of useful symmetry properties, and the reader is encouraged to consult [27] for them. Most importantly, both the metric and the Ricci tensor are symmetric tensors.

The Einstein tensor constitutes the geometric part of the Einstein equation [27]

$$G_{\mu\nu} = 8\pi T_{\mu\nu}. \tag{6}$$

The right hand side of the equation is determined by the matter content of the spacetime, and $T_{\mu\nu}$ is the energy-momentum tensor. While $T_{\mu\nu}$ can in principle be rather complicated, in cosmology matter can be treated as an ideal fluid to a very good approximation [27]. In this case, the energy-momentum tensor takes the simple form

$$T_{\mu\nu} = (\rho + p) u_\mu u_\nu + p g_{\mu\nu}, \tag{7}$$

where ρ and p are the energy density and pressure measured in the rest frame and u^μ is the 4-velocity [27]. The dynamics of matter are given by the continuity equation $\nabla_\mu T^{\mu\nu} = 0$, where ∇ is the covariant derivative [27].

As I noted in the introduction, the main assumption usually made in cosmology is that on a large enough scale the universe is both homogeneous and isotropic. This assumption breaks obviously on the smaller scales, and the majority of this thesis is dedicated to solving the full system of Einstein equations numerically. However, the homogeneous and isotropic solution serves as a useful background solution for both the perturbation theory and the full relativistic equations.

With the assumption of homogeneity and isotropy there is always a coordinate system in which the metric takes the form

$$ds^2 = -dt^2 + a^2(t)\left(\frac{dr^2}{1-kr^2} + r^2 d\theta^2 + r^2 \sin^2\theta d\phi^2\right), \tag{8}$$

where $a(t)$ is the scale factor and k is the spatial curvature parameter [27]. This metric is called the Friedmann-Lemaître-Robertson-Walker -metric (FLRW-metric). The flat FLRW-universe is the special case of zero curvature. The assumption of homogeneity and isotropy also prohibits any peculiar velocity[3] for the matter content, and so in this coordinate system the 4-velocity of the matter content is just $u^\mu = (1{,}0{,}0{,}0)$ [27]. In turn, the components of the energy-momentum tensor reduce into $T^{\mu\nu} = \text{diag}(\rho,p,p,p)$, where ρ and p are by assumption constants in space.

Calculating the components of the Einstein tensor and plugging the results in the Eisntein equation yields the Friedmann equations [27]

$$\frac{\dot{a}^2}{a^2} = \frac{8\pi\rho}{3} - \frac{k}{a^2} \tag{9}$$

$$\frac{\ddot{a}}{a} = -\frac{4\pi(\rho+3p)}{3}, \tag{10}$$

and continuity equation takes the form [27]

$$\dot{\rho} = -3\frac{\dot{a}}{a}(\rho + p). \tag{11}$$

However, these equations are not yet closed by themselves, as an equation of state $p = p(\rho)$ is still needed. The equation of state is usually written as $p = w\rho$, where

---

[3] Peculiar velocity: Velocity not arising from the expansion of the universe.

w is a constant in the most common applications. The choices most relevant for cosmology are $w = 0$ for pressureless matter, often called dust, $w = 1/3$ for radiation and $w = -1$ for dark energy [27].

One could continue from here and solve the Friedmann equations for a multiple-component fluid. However, in this thesis I will deal solely with the Einstein-de Sitter -universe, or a spatially flat matter dominated universe. Thus, I will set $w = 0$ and $k = 0$. The corresponding solutions the Friedmann equations and the continuity equation are

$$a(t) = a_0 (t/t_0)^{2/3} \tag{12}$$

and

$$\rho(a) = \rho(a_0)(a_0/a)^3, \tag{13}$$

where a_0, t_0 and $\rho(a_0)$ are arbitrary constants. The rate of expansion for a FLRW-universe is usually characterized by the Hubble rate $H = \dot{a}/a$ [4]. In an Einstein-de Sitter -universe the Hubble rate is given by

$$H_{EdS} = \frac{2}{3t} = \frac{2}{3t_0}\left(\frac{a}{a_0}\right)^{-3/2}. \tag{14}$$

In most applications the scale factor is a monotonous function of coordinate time and it serves as a natural choice of time parameter. However, in cosmology it is customary to parametrize time in terms of the redshift z. The frequency of light changes due to the expansion of the FLWR-universe as

$$z = \frac{\omega_{sr} - \omega_{obs}}{\omega_{obs}} = \frac{a_{obs}}{a_{sr}} - 1, \tag{15}$$

where ω_{sr}, ω_{obs}, a_{sr} and a_{obs} are the frequency of the radiation and the scale factor at the source and the observer respectively. While this is a standard expression [4], I will discuss redshift in a more general context in section 6.2.

2.3 Cosmological perturbation theory

By definition, the homogeneous and isotropic model of the universe cannot account for many phenomena such as structure formation. The full inhomogeneous Einstein equations are usually too complicated to solve analytically, and the traditional way to deal with this is linear perturbation theory. I will again only give the most relevant results of perturbation theory, and the reader can find the full calculation in [5, 6].

In principle, linear cosmological perturbation theory is very straightforward. The linearized equations are found simply by choosing a background metric which solves the Einstein equations, writing the full metric as a sum of the background and a perturbation and dropping the higher order terms from the Einstein equations. A similar split is introduced with all fields defined on the spacetime. However, it turns out that this split into the perturbation and the background is dependent on the chosen coordinate system, or gauge dependent, which introduces some subtlety into the picture.

Split the metric as $g_{\mu\nu}(t,\vec{x}) = \bar{g}_{\mu\nu}(t) + \delta g_{\mu\nu}(t,\vec{x})$. The most common background used in cosmology is the spatially flat FLRW-metric, and here I will always assume that the background quantities are constants in space. The gauge dependence of the split can be seen by considering the infinitesimal coordinate transformation $x^\mu \to \tilde{x}^\mu = x^\mu + \zeta^\mu$. The metric transforms in the usual way [27],

$$\tilde{g}_{\mu\nu}(\tilde{x}) = \frac{\partial x^\alpha}{\partial \tilde{x}^\mu}\frac{\partial x^\beta}{\partial \tilde{x}^\nu} g_{\alpha\beta}(x), \tag{16}$$

and expanding the left hand side to the first order in ζ^μ results in

$$\tilde{g}_{\mu\nu}(\tilde{x}) = \bar{g}_{\mu\nu}(\tilde{t}) + \delta\tilde{g}_{\mu\nu}(\tilde{x}) = \bar{g}_{\mu\nu}(t) + \zeta^0 \partial_0 \bar{g}_{\mu\nu}(t) + \delta\tilde{g}_{\mu\nu}(\tilde{x}). \tag{17}$$

Solving for the transformed perturbation and plugging in the partial derivatives leaves to first order

$$\delta\tilde{g}_{\mu\nu}(\tilde{x}) = \delta g_{\mu\nu}(x) - \zeta^0 \partial_0 \bar{g}_{\mu\nu}(t) - 2\bar{g}_{\alpha(\mu}\partial_{\nu)}\zeta^\alpha. \tag{18}$$

The gauge transformation rules for tensors of other ranks can be derived in an analogous way [5]. It is worth noting that even the perturbations of scalar quantities are gauge dependent.

The next step after choosing the background split is to write the evolution equations for the perturbations [5]. The background must satisfy the Einstein equations $\bar{G}_{\mu\nu} = 8\pi\bar{T}_{\mu\nu}$, where $\bar{G}_{\mu\nu}$ and $\bar{T}_{\mu\nu}$ are the background Einstein tensor and energy-momentum tensor respectively. As such, the evolution equations are found simply by calculating the perturbations of the tensors and equating them $\delta G_{\mu\nu} = 8\pi\delta T_{\mu\nu}$. Similarly, expanding the continuity equations to first order results in $\nabla_\mu \delta T^{\mu\nu} = 0$.

The evolution equations can naturally be written in many different forms. The most widely used one is to decompose the metric perturbations into the scalar, vector and tensor parts as each of these components evolve independently of each other. This approach is detailed in most textbooks on the subject, for example [6].

However, the aim in this text is to eventually write down the full Einstein equations and the linear perturbation theory serves mainly for comparing their solutions to the linear approximation. The usual decomposition makes this comparison somewhat more complicated than necessary. For my purposes it is sufficient to fix a gauge at the beginning and write the evolution equations for the metric components directly.

It is always possible to find a gauge transformation which sets $g_{0i} = 0$ and $g_{00} = -1$ [5]. This gauge choice is called the synchronous gauge. In fact, this is not only possible in linear theory, but it also extends to the full theory as well. This is the gauge I will choose with the full Einstein equations later on.

The reader can find the calculation for the synchronous gauge perturbation equations with ideal fluid matter in [5]. I denote $\delta g_{ij} = a^2 h_{ij}$ and in order to condense the notation, I will be implicitly summing over all repeated indices regardless of their position. For instance, I will denote $h = h_{ii} := \sum_i h_{ii}$. I will also split the rest frame energy density as

$$\rho = \bar{\rho}(1+\delta). \tag{19}$$

The linear perturbation equations read

$$\frac{1}{2}\ddot{h} + \frac{\dot{a}}{a}\dot{h} = 4\pi\bar{\rho}(1+c_s)\delta \tag{20}$$

$$\dot{h}_{,i} - \dot{h}_{ij,j} = -16\pi\bar{\rho}(1+w)av^i \tag{21}$$

$$R^{(3)}_{ij} - a^2\left[\frac{3}{2}\frac{\dot{a}}{a}\dot{h}_{ij} + \frac{1}{2}\frac{\dot{a}}{a}\dot{h}\delta_{ij} + \frac{1}{2}\ddot{h}_{ij}\right] = 4\pi a^2\delta_{ij}\bar{\rho}(1-c_s)\delta, \tag{22}$$

where $c_s^2 = \partial p/\partial\rho$ is the speed of sound, v^i is the peculiar velocity of the fluid and

$w = p/\rho$ is the ratio of the pressure and the energy energy density [5]. Here $R_{ij}^{(3)}$ is the three-dimensional Ricci tensor calculated using only the spatial part of the metric.

The continuity equations can be linearized in the same way, resulting in the equations

$$\dot{\delta} + (1+w)(\theta - \dot{h}/2) = 3\frac{\dot{a}}{a}(w - c_s^2)\delta \tag{23}$$

$$\frac{\partial}{\partial t}\left[(1+w)\theta\right] + (2-3w)(1+w)\theta\frac{\dot{a}}{a} = -c_s^2\nabla^2\left(\frac{\delta}{a^2}\right), \tag{24}$$

where $\theta = \partial_i v^i/a$ is the expansion parameter [5]. Note that for a pressureless fluid $c_s = 0$ and with this choice $v^i \equiv 0$ solves equation 24. The system never develops peculiar velocity in the synchronous gauge if the velocity vanishes at the initial time. This property will turn out to be of use with the full Einstein equations as well.

3 ADM-formalism

Einstein's field equations in the form of equation 6 do not immediately lend themselves to numerical solutions. In order to proceed, the equations should be written in the so called 3+1-form by choosing a time coordinate and solving for the time derivatives. One of the original formulations in this vein was done by Arnowitt, Deser and Misner in 1959, and the resulting equations are often called the ADM-equations [17]. I will not follow this original formulation. Instead, this section will closely follow an equivalent derivation by Baumgarte and Shapiro in [18].

3.1 Deriving the ADM-equations

I begin by assuming that there exists a global time function t such that its set of level surfaces covers the entire spacetime[4]. From now on these level surfaces will be called timeslices. The tangent spaces to the timeslices can be characterized by the gradient one-form

$$\Omega_\mu = \nabla_\mu t, \tag{25}$$

and a normal vector to the surface is found by raising its index using the metric. The rate of change of t for an observer with the velocity Ω^μ is determined by the length of the vector. It is useful to define the lapse function α by

$$\Omega_\mu \Omega^\mu = -\frac{1}{\alpha^2} \tag{26}$$

and the unit normal vector

$$n^\mu = -\alpha \Omega^\mu. \tag{27}$$

The lapse function is always taken to be positive. Note that $n_\mu n^\mu = -1$ by definition.

Constructing the spatial metric $\gamma_{\mu\nu}$ on a timeslice is now simple. The length of a curve calculated with the spatial metric on a timeslice should be the same as when measured using the full metric $g_{\mu\nu}$. Moreover, the t-component of $\gamma_{\mu\nu}$ should vanish,

---

[4] Mathematically speaking, I assume that the solution manifold allows a foliation. For more information on the underlying mathematics the reader can consult [28].

that is $n^\mu \gamma_{\mu\nu} = 0$. The spatial metric must then be the projection operator

$$\gamma_{\mu\nu} = g_{\mu\nu} + n_\mu n_\nu. \tag{28}$$

It is simple to verify that $\gamma^{\mu\nu}$ is the inverse to $\gamma_{\mu\nu}$. Note that raising and lowering indices is always done using the full metric. However, if the tensor being operated on is purely spatial, that is $n^\mu T_{\mu\nu} = 0$ for all indices with obvious generalizations to other ranks, the same result is obtained by using the spatial metric as well.

The timeslice equipped with the spatial metric is a Riemannian submanifold and so covariant derivatives and curvature can be defined in the usual way [18]. I define the covariant derivative D on the timeslice to be torsionless and compatible with the spatial metric. The Christoffel symbols associated with D are then [18]

$$\Gamma^\mu_{\alpha\beta} = \frac{1}{2}\gamma^{\mu\nu}(\partial_\alpha \gamma_{\nu\beta} + \partial_\beta \gamma_{\nu\alpha} - \partial_\nu \gamma_{\alpha\beta}). \tag{29}$$

The spatial Riemann tensor, Ricci tensor and the Ricci scalar are defined analogously to their four-dimensional counterparts. From now on the $R^\mu{}_{\nu\alpha\beta}$ will refer to the spatial tensor and the notation ${}^{(4)}R^\mu{}_{\nu\alpha\beta}$ is used for the four-dimensional version. I will use a similar notation for other tensors as well.

Since the spatial metric is a projection of the full metric on a timeslice, it is clear that it is missing some of the information necessary to construct the full metric. In particular, while the spatial metric contains all information on the intrinsic curvature of the timeslices, it doesn't constrain how the timeslices are embedded in the four-dimensional spacetime [18]. Thus, I still need another object for that purpose, namely the extrinsic curvature.

I define the extrinsic curvature tensor $K_{\mu\nu}$ as

$$K_{\mu\nu} = -\gamma_\mu{}^\alpha \gamma_\nu{}^\beta \nabla_\alpha n_\beta. \tag{30}$$

Next, note that $n_{[\alpha}\nabla_\mu n_{\nu]} = 0$, which can be seen by explicitly writing n_α in terms of derivatives of t. The antisymmetric part of the extrinsic curvature is

$$\begin{aligned} K_{[\mu\nu]} = \frac{1}{2}\,[&\nabla_\mu n_\nu - \nabla_\nu n_\mu + n^\alpha n_\nu \nabla_\mu n_\alpha - n^\alpha n_\mu \nabla_\nu n_\alpha \\ &+ n^\alpha n_\nu \nabla_\alpha n_\mu - n^\alpha n_\mu \nabla_\alpha n_\nu] \qquad (31) \\ = -3&n^\alpha n_{[\alpha}\nabla_\mu n_{\nu]} = 0. \qquad (32) \end{aligned}$$

Like the metric, the extrinsic curvature is then a symmetric tensor. The extrinsic curvature can be written in a more easily interpreted form using the Lie derivative [27]. Consider the Lie derivative of the spatial metric:

$$\mathcal{L}_n \gamma_{\mu\nu} = \mathcal{L}_n (g_{\mu\nu} + n_\mu n_\nu) = 2\nabla_{(\mu} n_{\nu)} + n_\mu \mathcal{L}_n n_\nu + n_\nu \mathcal{L}_n n_\mu, \tag{33}$$

where I used the product rule and substituted in the expression for the Lie derivative of the metric [27]. Expanding the Lie derivatives, [27]

$$\mathcal{L}_n n_\nu = n^\alpha \nabla_\alpha n_\nu + n_\alpha \nabla_\nu n^\alpha, \tag{34}$$

and noting that the latter term vanishes results in

$$\begin{align} \mathcal{L}_n \gamma_{\mu\nu} &= 2(\nabla_{(\mu} n_{\nu)} + n_{(\mu|} n^\alpha \nabla_\alpha n_{|\nu)}) \tag{35} \\ &= \Big((\delta^\alpha_\mu + n^\alpha n_\mu)(\delta^\beta_\nu + n^\beta n_\nu) \nabla_\alpha n_\beta\Big) + (\mu \leftrightarrow \nu) \tag{36} \\ &= -2K_{(\mu\nu)} = -2K_{\mu\nu}. \tag{37} \end{align}$$

Since the Lie derivative $\mathcal{L}_n$ acts like a directional derivative of an object along the flow generated by the normal vector field n, the extrinsic curvature measures how much the spatial metric deforms between timeslices.

The next step is to write the Einstein equation in terms of the spatial metric and the extrinsic curvature. All information about the four-dimensional curvature can be expressed through different projections of the Riemann tensor [18]. These projections can be expressed in terms of the spatial tensors through the equations of Gauss, Codazzi and Ricci. The derivation for each of these equations can be found in [18, 28] and the equations read:

$$\begin{align} R_{\mu\nu\alpha\beta} + K_{\mu\nu}K_{\alpha\beta} - K_{\mu\beta}K_{\nu\alpha} &= {\gamma_\mu}^\lambda {\gamma_\nu}^\rho {\gamma_\alpha}^\zeta {\gamma_\beta}^{\chi\,(4)} R_{\lambda\rho\zeta\chi} \text{ (Gauss' equation)} \tag{38} \\ D_\nu K_{\mu\alpha} - D_\mu K_{\nu\alpha} &= {\gamma_\mu}^\lambda {\gamma_\nu}^\rho {\gamma_\alpha}^\zeta n^{\chi\,(4)} R_{\lambda\rho\zeta\chi} \text{ (Codazzi equation)} \tag{39} \\ \mathcal{L}_n K_{\mu\nu} = n^\alpha n^\lambda {\gamma_\mu}^\beta {\gamma_\nu}^{\rho\,(4)} R_{\alpha\beta\lambda\rho} &- \frac{1}{\alpha} D_\mu D_\nu \alpha - {K^\alpha}_\nu K_{\mu\alpha}. \text{(Ricci equation)} \tag{40} \end{align}$$

The first two equations consist only of objects on one timeslice and cannot therefore describe the evolution of the metric at different times. These constraint equations should be satisfied on each timeslice separately. The Ricci equation in turn determines the evolution of the extrinsic curvature due to the Lie derivative.

The spatial Ricci tensor and scalar are found easiest by contracting the Gauss' equation. The resulting expressions are

$$\gamma^{\alpha\beta}\gamma^{\lambda}{}_{\mu}\gamma^{\rho}{}_{\nu}\,{}^{(4)}R_{\alpha\lambda\beta\rho} = R_{\mu\nu} + KK_{\mu\nu} - K^{\alpha}{}_{\nu}K_{\alpha\mu}, \tag{41}$$

$$\gamma^{\alpha\beta}\gamma^{\lambda\rho\,(4)}R_{\alpha\lambda\beta\rho} = R + K^2 - K_{\alpha\beta}K^{\alpha\beta}. \tag{42}$$

The left hand side of the latter equation can be expressed using the four-dimensional Ricci tensor and scalar by expanding the spatial metrics, resulting in

$$\gamma^{\alpha\beta}\gamma^{\lambda\rho\,(4)}R_{\alpha\lambda\beta\rho} = (g^{\alpha\beta} + n^{\alpha}n^{\beta})(g^{\lambda\rho} + n^{\lambda}n^{\rho})^{(4)}R_{\alpha\lambda\beta\rho} = {}^{(4)}R + 2n^{\alpha}n^{\beta\,(4)}R_{\alpha\beta}. \tag{43}$$

The term with four normal vectors vanishes due to the antisymmetric indices of the Riemann tensor. Noting that $n^{\alpha}n^{\beta}g_{\alpha\beta} = -1$, the right hand side of equation 43 can be written as

$$2n^{\alpha}n^{\beta}\left({}^{(4)}R_{\alpha\beta} - \frac{1}{2}{}^{(4)}Rg_{\alpha\beta}\right) = 2n^{\alpha}n^{\beta}G_{\alpha\beta}. \tag{44}$$

Then, the contracted Gauss' equation is

$$R + K^2 - K_{\alpha\beta}K^{\alpha\beta} = 2n^{\alpha}n^{\beta}G_{\alpha\beta} = 16\pi n^{\alpha}n^{\beta}T_{\alpha\beta} = 16\pi\tilde{\rho}, \tag{45}$$

where $\tilde{\rho} = n_{\alpha}n_{\beta}T^{\alpha\beta}$ is the energy density measured by a normal observer. Equation 45 is called the Hamiltonian constraint.

Another constraint equation is obtained by contracting the Codazzi equation. The contraction reads

$$D_{\alpha}K_{\mu}{}^{\alpha} - D_{\mu}K = \gamma^{\alpha}{}_{\mu}\gamma^{\beta\lambda}n^{\rho\,(4)}R_{\alpha\beta\lambda\rho} = -\gamma^{\alpha}{}_{\mu}(g^{\beta\lambda} + n^{\beta}n^{\lambda})n^{\rho\,(4)}R_{\beta\alpha\lambda\rho}. \tag{46}$$

The latter term again vanishes due to the antisymmetry of the Riemann tensor, leaving

$$D_{\alpha}K_{\mu}{}^{\alpha} - D_{\mu}K = -\gamma^{\alpha}{}_{\mu}n^{\beta\,(4)}R_{\alpha\beta}. \tag{47}$$

Note next that $\gamma^{\alpha}{}_{\mu}n^{\beta}g_{\alpha\beta} = 0$, and so the right hand side can again be expressed as a contraction of the Einstein tensor, $\gamma^{\alpha}{}_{\mu}n^{\beta\,(4)}R_{\alpha\beta} = \gamma^{\alpha}{}_{\mu}n^{\beta}G_{\alpha\beta} = 8\pi\gamma^{\alpha}{}_{\mu}n^{\beta}T_{\alpha\beta}$. Defining the momentum density measured by a normal observer S_{μ} as [18]

$$S_{\mu} = -\gamma^{\alpha}{}_{\mu}n^{\beta}T_{\alpha\beta} \tag{48}$$

results in the constraint equation

$$D_\alpha K_\mu{}^\alpha - D_\mu K = 8\pi S_\mu. \tag{49}$$

This equation is called the momentum constraint.

The last remaining pieces are the evolution equations themselves. The spatial metrics between different timeslices are connected by equation 37, the definition of the extrinsic curvature. The Ricci equation then completes the system of equations.

There is still one more contraction of the four-dimensional Riemann tensor to deal with in the Ricci equation. However, the contraction is simple to express in a form that has already been calculated:

$$\begin{aligned} n^\alpha n^\beta \gamma_\mu{}^\lambda \gamma_\nu{}^\rho {}^{(4)}R_{\alpha\lambda\beta\rho} &= (\gamma^{\alpha\beta} - g^{\alpha\beta})\gamma_\mu{}^\lambda \gamma_\nu{}^\rho {}^{(4)}R_{\alpha\lambda\beta\rho} \\ &= \gamma^{\alpha\beta}\gamma_\mu{}^\lambda \gamma_\nu{}^\rho {}^{(4)}R_{\alpha\lambda\beta\rho} - \gamma_\mu{}^\alpha \gamma_\nu{}^\beta {}^{(4)}R_{\alpha\beta}. \end{aligned} \tag{50}$$

The first term is just the left hand side of the once-contracted Gauss' equation. Substituting in that along with the Einstein equation results in

$$n^\alpha n^\beta \gamma_\mu{}^\lambda \gamma_\nu{}^\rho {}^{(4)}R_{\alpha\lambda\beta\rho} = R_{\mu\nu} + KK_{\mu\nu} - K_{\mu\alpha}K^\alpha{}_\nu - 8\pi\gamma_\mu{}^\alpha\gamma_\nu{}^\beta(T_{\alpha\beta} - \frac{1}{2}g_{\alpha\beta}T). \tag{51}$$

This can be expressed in a more compact form by defining the spatial stress tensor and its trace as $S_{\mu\nu} = \gamma_\mu{}^\alpha\gamma_\nu{}^\beta T_{\alpha\beta}$ and $S = S^\alpha{}_\alpha$.

In its current form the Ricci equation and equation 37 describe the evolution of $\gamma_{\mu\nu}$ and $K_{\mu\nu}$ along the integral curve of the vector field n^μ. However, the rate of change of t along these integral curves is given by $n^a \nabla_a t = 1/\alpha$. In particular, the rate of change is not a constant in space for a general α, and therefore points at different spatial points end up in different timeslices after evolving the same length on the integral curve.

This problem can be solved by defining another vector field $t^\mu = \alpha n^\mu + \beta^\mu$, where β^μ is any spatial vector field, $n^\mu \beta_\mu = 0$. The field β^μ is called the shift vector. The rate of change along the integral curves of t^μ is now a constant, $t^\mu \Omega_\mu = 1$, and thus $\mathcal{L}_t$ is a suitable time derivative. Due to the linearity of the Lie derivative [27], $\mathcal{L}_t$ can be written as

$$\mathcal{L}_t K_{\mu\nu} = \alpha \mathcal{L}_n K_{\mu\nu} + \mathcal{L}_\beta K_{\mu\nu}, \tag{52}$$

and so the Ricci equation becomes

$$\begin{aligned}\mathcal{L}_t K_{\mu\nu} = &-D_\mu D_\nu \alpha + \alpha\left(R_{\mu\nu} - 2K_{\mu\alpha}K^{\alpha}{}_{\nu} + KK_{\mu\nu}\right) \\ &- 8\pi\alpha\left(S_{\mu\nu} - \frac{1}{2}\gamma_{\mu\nu}(S - \tilde{\rho})\right) + \mathcal{L}_\beta K_{\mu\nu}.\end{aligned} \tag{53}$$

The evolution equation for the spatial metric can be treated in the same way,

$$\mathcal{L}_t \gamma_{\mu\nu} = -2\alpha K_{\mu\nu} + \mathcal{L}_\beta \gamma_{\mu\nu}. \tag{54}$$

There is still one more simplification that can be done. Note that all tensors involved in the constraint and the evolution equations are spatial. Therefore the amount of non-zero components can be reduced by choosing a suitable coordinate system. As expected, this coordinate system involves using t as the time coordinate.

The observers stationary with respect to this coordinate system are moving along the integral curves of the vector field t^μ. The components of t^μ in this coordinate system must then be $t^\mu = (1,0,0,0)$. The other coordinates should specify the location of a point on each timeslice, and as such the rest of the coordinate basis vectors $e^{\mu}_{(i)}$ must be purely spatial. Such a coordinate frame is constructed explicitly in [18].

An immediate consequence of this is that $n_\alpha e^{\alpha}_{(i)} = 0$, and so in this coordinate system $n_a = (n_0,0,0,0)$. The contravariant components of n^μ are simple to find using the definition of t^μ to get $n^\mu = (t^\mu - \beta^\mu)/\alpha$. Since β^μ is a spatial vector, $n_\alpha \beta^\alpha = n_0 \beta^0 = 0$, and the components of the shift vector must be $\beta^\mu = (0,\beta^i)$. The resulting contravariant components are

$$n^\mu = (\alpha^{-1},\alpha^{-1}\beta^i), \tag{55}$$

and using the normalization $n_\alpha n^\alpha = -1$ the covariant components reduce into

$$n_\mu = (\alpha,0,0,0). \tag{56}$$

This in turn implies that the zeroth components of any contravariant spatial tensor must vanish.

In particular, the spatial metric and the extrinsic curvature have $\gamma^{0\mu} = 0$ and $K^{0\mu} = 0$ for all μ, which reduces the number of independent components each has from ten to six. The spatial components of the metric are just $\gamma_{ij} = g_{ij} + n_i n_j = g_{ij}$.

In this coordinate system, γ^{ij} is the matrix inverse of γ_{ij}:

$$\begin{aligned}\delta^i_j = g^{i\mu} g_{\mu j} &= (\gamma^{i\mu} - n^\mu n^i)(\gamma_{\mu j} - n_\mu n_j) && (57)\\ &= \gamma^{i\mu}\gamma_{\mu j} - n^i n_j = \gamma^{ik}\gamma_{kj}. && (58)\end{aligned}$$

The full metric can then be written using $g^{ab} = \gamma^{ab} - n^a n^b$ and inverting the matrix. The resulting metric is

$$ds^2 = -\alpha^2 dt^2 + \gamma_{ij}(dx^i + \beta^i dt)(dx^j + \beta^j dt). \tag{59}$$

I can now finally write the ADM-equations. As the Lie derivative $\mathcal{L}_t$ acts as the derivative along the integral curves of t^a, it can be written as just the time derivative ∂_t [27]. Also, all temporal terms vanish in contractions between spatial tensors, and it is sufficient to sum over the spatial indices. Collecting the relevant equations and expanding the Lie derivatives with respect to the shift $\mathcal{L}_\beta$ results in [18]

$$\begin{aligned}&\partial_t \gamma_{ij} = -2\alpha K_{ij} + D_i\beta_j + D_j\beta_i, && (60)\\ &\partial_t K_{ij} = -D_i D_j \alpha + \alpha(R_{ij} - 2K_{ik}K^k{}_j + KK_{ij}) - 8\pi\alpha(S_{ij} - \frac{1}{2}\gamma_{ij}(S - \tilde{\rho}))\\ &\qquad + \beta^k D_k K_{ij} + K_{ik} D_j \beta^k + K_{jk} D_i \beta^k, && (61)\\ &R + K^2 - K_{ij}K^{ij} = 16\pi\tilde{\rho}, && (62)\\ &D_j(K^{ij} - \gamma^{ij}K) = 8\pi S^i. && (63)\end{aligned}$$

Taking the trace of equation 61 and substituting the momentum constraint for the Ricci scalar results in the evolution equation for the trace of the extrinsic curvature,

$$\partial_t K = -D^2\alpha + \alpha(K_{ij}K^{ij} + 4\pi(\bar{\rho} + S)) + \beta^i D_i K. \tag{64}$$

While this equation is not necessary to evolve the metric, it will turn out to be of use later.

3.2 Fluid equations and fixing the gauge

The ADM-equations by themselves are not enough to close the system of equations. The missing piece are the fluid equations governing the dynamics of the energy-momentum tensor. As I will only consider matter dominated systems in this project, I will set $p = 0$ from now on. I will also write the 4-velocity as $u^a = \gamma_v(\alpha^{-1}, v^i)$, where $\gamma_v = (1 - v_i v^i)^{-1/2}$ is the Lorentz factor and v^i is the peculiar 3-velocity [47]. With this notation the energy-momentum tensor of an ideal fluid has the components

$$T^{\mu\nu} = \rho u^\mu u^\nu = \begin{pmatrix} \rho\gamma_v^2/\alpha^2 & \rho\gamma_v^2 v^i/\alpha \\ \rho\gamma_v^2 v^j/\alpha & \rho\gamma_v^2 v^i v^j \end{pmatrix}. \tag{65}$$

After some effort expanding the continuity equation $\nabla_\alpha T^{\alpha\mu} = 0$ results in the equations

$$\begin{aligned} \dot{v}^k = & -v^i v^j \alpha(\Gamma^k_{ij} + v^k K_{ij}) + v^i(2\alpha K_i{}^k - v^k_{,i}\alpha - v^k \alpha_{,i}) \\ & - \gamma^{ki}\alpha_{,i} - 2v^k\dot{\alpha}/\alpha \end{aligned} \tag{66}$$

and

$$\begin{aligned} \dot{\rho} = & -2\rho\gamma_v^2\gamma_{ij}v^i\dot{v}^j + \alpha\rho(1 + 2\gamma_v^2)K_{ij}v^i v^j + 2\rho\dot{\alpha}/\alpha \\ & - \Gamma^i_{ij}\rho\alpha v^j + \alpha K\rho - \alpha(v^i\rho_{,i} + \rho v^i_{,i}) - 2\alpha\rho v^i\gamma_{v,i}/\gamma_v. \end{aligned} \tag{67}$$

As I mentioned when discussing linear perturbation theory, in this project I will be adopting the synchronous gauge by setting $\alpha \equiv 1$. For simplicity, I will also set $\beta^i \equiv 0$, which implies $t^\mu = n^\mu$. I will refer to the resulting coordinate system as the comoving coordinates.

The normal energy density is $\tilde{\rho} = T^{00}$ as expected, which can be expressed in terms of the usual rest frame energy density ρ as

$$\tilde{\rho} = \rho u^0 u^0 = \gamma_v^2 \rho. \tag{68}$$

The momentum density is in turn

$$\begin{aligned} S_i &= -\gamma_{i\mu} n_\nu T^{\mu\nu} = -\alpha\gamma_{i\mu}T^{\mu 0} = -\gamma_{ij}T^{j0} && (69) \\ &= -\gamma_{ij}\left(\rho u^0 u^j\right) = -\rho\gamma_v^2 v_i. && (70) \end{aligned}$$

where I used the fact that $\gamma_{i0} = g_{i0} + n_i n_0 = 0$ when $\beta_i = 0$. With similar calculations the spatial stress tensor and its trace can be written as

$$S_{ij} = v_i v_j \gamma_v^2 \rho, \tag{71}$$

$$S = v_i v^i \gamma_v^2 \rho. \tag{72}$$

Substituting the gauge choice into the evolution equation for the peculiar fluid velocity results in

$$\dot{v}^k = -v^i v^j (\Gamma^k_{ij} + v^k K_{ij}) + 2v^i K_i{}^k - v^i v^k_{,i}. \tag{73}$$

Note that every term in the above equation is proportional to the velocity itself. As was the case with the linear perturbation theory, the system cannot develop peculiar velocity in the synchronous gauge if the velocity is zero at the initial timeslice. Then, with a suitable choice of initial conditions I can set $v^i \equiv 0$. With our gauge choice and zero velocity the evolution equations reduce into

$$\dot{\gamma}_{ij} = -2K_{ij} \tag{74}$$

$$\dot{K}_{ij} = R_{ij} - 2K_{ik}K^k{}_j + KK_{ij} - 4\pi\rho\gamma_{ij} \tag{75}$$

$$\dot{\rho} = K\rho. \tag{76}$$

3.3 ADM-equations for perturbations

Even the simple form of the ADM-equations with the fixed gauge is still not usable in a numerical calculation. The initial conditions I will be using in this project consist of a spatially flat FLRW-background with a small perturbation on top of it. I will discuss this in more detail in section 5. The problem arises with the spatial derivatives in the evolution equations and the Ricci tensor in particular. As the spatial derivatives must be calculated numerically, the numerical error will be prohibitively large relative to the size perturbation at early times.

In order to address this problem, I will now split the equations into the background part and the perturbation. Note that as with linear perturbation theory, this split is gauge dependent. I will avoid the problem of gauge transformations by only considering the gauge choice discussed above.

I define the split metric as

$$\gamma_{ij} = a^2(\delta_{ij} + \delta\gamma_{ij}), \tag{77}$$

where a is the scale factor for the flat Einstein-de Sitter -universe. The time derivative of γ_{ij} reads

$$\dot{\gamma}_{ij} = 2a\dot{a}\gamma_{ij} + a^2\delta\dot{\gamma}_{ij} \tag{78}$$

and comparing this with the evolution equation for γ_{ij} suggests that the extrinsic curvature should be split as

$$K_{ij} = -a\dot{a}(\delta_{ij} + \delta K_{ij}). \tag{79}$$

For the energy density, I take cue from the usual linear perturbation theory and write

$$\rho = \bar{\rho}(1 + \delta), \tag{80}$$

where $\bar{\rho}$ is the FLRW energy density. For convenience, I also define $\delta\tilde{\gamma}^{ij}$ such that

$$\gamma^{ij} = a^{-2}(\delta^{ij} + \delta\tilde{\gamma}^{ij}). \tag{81}$$

Note that $\delta\tilde{\gamma}^{ij}$ is not the matrix inverse of $\delta\gamma_{ij}$, but instead it must be solved from the equation $\gamma^{ij}\gamma_{jk} = \delta^i_k$ as

$$\delta\tilde{\gamma}^{ij} = -a^2\gamma^{ik}\delta\gamma_{kl}\delta^{lj}. \tag{82}$$

A simple calculation shows that entire background part of the evolution equations reduces into Friedmann equations and cancels. The remaining parts of the evolution equations describe the time evolution of the perturbations. I will again implicitly sum over all repeated indices in a term regardless of their position. The equations for the perturbations read

$$\begin{aligned}
\delta\dot{\gamma}_{ij} &= \frac{2\dot{a}}{a}\delta K_{ij} - \frac{2\dot{a}}{a}\delta\gamma_{ij}, && (83)\\
\delta\dot{K}_{ij} &= -\frac{1}{a\dot{a}}R_{ij} + \frac{\dot{a}}{a}\Big(\frac{1}{2}\delta K_{ij} + 2\delta\tilde{\gamma}^{ij} - \delta K_{aa}\delta_{ij} - \delta\tilde{\gamma}^{aa}\delta_{ij}\\
&\quad -\delta K_{aa}\delta K_{ij} - \delta\tilde{\gamma}^{aa}\delta K_{ij} - \delta\tilde{\gamma}^{kl}\delta K_{kl}\delta_{ij} + 2\delta K_{ik}\delta K_{kj}\\
&\quad +2\delta\tilde{\gamma}^{kl}\delta K_{lj}\delta_{ki} + 2\delta\tilde{\gamma}^{kl}\delta K_{li}\delta_{kj} + 2\delta\tilde{\gamma}^{kl}\delta K_{ik}\delta K_{lj} - \delta\tilde{\gamma}^{kl}\delta K_{kl}\delta K_{ij}\Big)\\
&\quad + 4\pi\bar{\rho}\frac{a}{\dot{a}}\left(\delta\delta_{ij} + \delta\gamma_{ij} + \delta\delta\gamma_{ij}\right), && (84)\\
\dot{\delta} &= -\frac{\dot{a}}{a}\left(\delta\tilde{\gamma}^{ii} + \delta K_{ii} + \delta\delta K_{ii} + \delta\delta\tilde{\gamma}^{ii} + \delta\tilde{\gamma}^{ij}\delta K_{ij} + \delta\delta\tilde{\gamma}^{ij}\delta K_{ij}\right). && (85)
\end{aligned}$$

It is not necessary to split the spatial Christoffel symbol and Ricci tensor, as the background is spatially flat on each timeslice.

The constraint equations split in the same way and the background terms cancel due to the Friedmann equations. The split Hamiltonian constraint becomes

$$\begin{aligned}
&R + \left(\frac{\dot{a}}{a}\right)^2 \Big[\delta K_{ii} + \delta\tilde{\gamma}^{ii} - \delta K_{ij}\delta K_{ij} - \delta\tilde{\gamma}^{ij}\delta K_{ij} - \delta\tilde{\gamma}^{ij}\delta\tilde{\gamma}^{ij}\\
&+(\delta K_{ii})^2 + (\delta\tilde{\gamma}^{ii})^2 + 2\delta\tilde{\gamma}^{ii}\delta K_{jj} + 2\delta\tilde{\gamma}^{kk}\delta\tilde{\gamma}^{ij}\delta K_{ij} + 2\delta K_{kk}\delta\tilde{\gamma}^{ij}\delta K_{ij}\\
&-2\delta\tilde{\gamma}^{ik}\delta\tilde{\gamma}^{kj}\delta K_{ij} - 2\delta\tilde{\gamma}^{ij}\delta K_{ik}\delta K_{kj} + (\delta\tilde{\gamma}^{ij}\delta K_{ij})^2 - \delta\tilde{\gamma}^{ik}\delta\tilde{\gamma}^{jl}\delta K_{ij}\delta K_{kl}\Big]\\
&= 16\pi\bar{\rho}\delta. \qquad (86)
\end{aligned}$$

With the gauge choice specified above and zero peculiar velocity the right hand side of the momentum constraint vanishes. The background part of the extrinsic curvature is a constant in space and the background spatial Christoffel symbols vanish. Thus, the background part of the momentum constraint is zero, and a split is not necessary in the equation.

This form of the ADM equations closely resembles the equations found using linear perturbation theory. The linear equations can be recovered from the ADM equations by eliminating the extrinsic curvature from the ADM equations by differentiating equation 83 and dropping the higher order terms. Equation 20 is found immediately by using the same procedure on the trace equation 64.

3.4 Issues with the ADM-formalism

Numerical implementations of the ADM-equations have seen some success in calculating the spacetime when the setup is simple enough. Spherical or cylindrical symmetry is often enough to ensure a numerically stable solution [18]. In particular, symmetries of the spacetime can allow substituting one or more constraint equations directly into the evolution equations, considerably improving the stability. For instance, the evolution of the LTB-spacetime can be calculated in this way [16].

However, when there are no applicable symmetries, the weaknesses of the ADM formulation are far more apparent. For example, the lack of stability in full three-dimensional black hole simulations was a long-standing problem in numerical relativity. The numerical issues can be traced back to the structure of the second order spatial derivatives in the ADM-equations. I will not go into the mathematical details in this text, and the reader will find more discussion on the topic in [18].

Luckily, the numerical stability of the Einstein equations depends heavily on the exact form of the second derivatives in the equations. This portion can be modified by adding zero to the equations in the form of the constraint equations, which has a large effect on the overall numerical behaviour [48]. An alternate formulation to the Einstein equations to address the issues will be discussed in the next section.

4 BSSN-formalism

The instability of the ADM-formalism has generally made it unusable for all but the most symmetric systems. As I mentioned in the introduction, the instability was a long standing problem in general relativity. For instance, calculating the accurate gravitational wave waveform was achieved only due to new developments during the past three decades [18, 22]. One solution to the problem is the so called Baumgarte-Shapiro-Shibata-Nakamura -formalism (BSSN-formalism). Even though the numerical implementation of the BSSN-equations will be left out of this thesis in order to manage its scope, I will still detail the formalism here for future use. The discussion here will closely follow the derivation by Baumgarte and Shapiro in [18]. Some additional details can be found in the original publications [19] and [20].

4.1 Deriving the BSSN-equations

The main issue with the stability of the ADM-formalism arises from the mixed spatial second derivative terms in the Ricci tensor [19]. The stability of the solution can be improved by rewriting the equations as a system of wave equations, which involves eliminating all second derivatives apart from the Laplace operator $\gamma^{kl}D_kD_l$ [18]. This will be achieved by promoting the troublesome terms into dynamical variables which will be evolved with their own equations.

I begin with a conformal transformation of the spatial metric,

$$\gamma_{ij} = e^{4\phi}\bar{\gamma}_{ij}, \tag{87}$$

where $\bar{\gamma}_{ij}$ is the conformally related metric. I choose the exponent as $\phi = \ln(\gamma)/12$, where γ is the determinant of the spatial metric. With this choice the determinant of the conformally related metric $\bar{\gamma}$ is unity.

It is also useful to split the extrinsic curvature into its trace and the traceless part

$$K_{ij} = A_{ij} + \frac{1}{3}\gamma_{ij}K, \tag{88}$$

where $K = \gamma^{ij} K_{ij}$. I will also conformally transform the traceless part

$$A_{ij} = e^{4\phi} \bar{A}_{ij} \tag{89}$$

so that the conformally related metric can be used to raise and lower indices of $\bar{A}_{ij}$. In particular $A^{ij} = e^{-4\phi} \bar{A}^{ij}$.

In order to continue, I need to rewrite the Ricci tensor and scalar in terms of the conformal factor and the conformally related metric. Plugging the conformal transformation into the Christoffel symbol in equation 4 results in

$$\Gamma^i_{jk} = \bar{\Gamma}^i_{jk} + 2(\delta^i_j \bar{D}_k \phi + \delta^i_k \bar{D}_j - \bar{\gamma}_{jk} \bar{\gamma}^{il} \bar{D}_l \phi). \tag{90}$$

Here $\bar{\Gamma}^i_{jk}$ are obtained by substituting the conformally related metric into equation 4 and $\bar{D}$ is the covariant derivative associated with these conformally related Christoffel symbols. Note that just as the spatial covariant derivative is defined as metric compatible with γ_{ij}, $\bar{D}$ is compatible with the conformally related metric, that is $\bar{D}_k \bar{\gamma}_{ij} = 0$. The proof for these identities is identical to the case with the full spatial metric.

It is clear from the conformal transformation of the Christoffel symbols that the Ricci tensor must transform as $R_{ij} = \bar{R}_{ij} + R^{\phi}_{ij}$, where $\bar{R}_{ij}$ is the Ricci tensor constructed using the conformally related Christoffel symbols and R^{ϕ}_{ij} contains the remaining terms. A lengthy but straightforward calculation gives the full expression,

$$R^{\phi}_{ij} = -2(\bar{D}_i \bar{D}_j \phi + \bar{\gamma}_{ij} \gamma^{lm} \bar{D}_l \bar{D}_m \phi) + 4((\bar{D}_i \phi)(\bar{D}_j \phi) - \bar{\gamma}_{ij} \bar{\gamma}^{lm} (\bar{D}_l \phi)(\bar{D}_m \phi)). \tag{91}$$

It will be useful later on to calculate a similar split for the Ricci scalar. The result is

$$R = \gamma^{ij} R_{ij} = e^{-4\phi} \left[\bar{R} - 8 \bar{\gamma}^{ij} (\bar{D}_i \bar{D}_j \phi + (\bar{D}_i \phi)(\bar{D}_j \phi)) \right], \tag{92}$$

where $\bar{R} = \bar{\gamma}^{ij} \bar{R}_{ij}$.

The most troublesome terms with mixed derivatives can be found in $\bar{R}_{ij}$ and more specifically in the terms involving the derivatives of the barred Christoffel symbols.

Expanding the Christoffel symbols and reordering the terms yields

$$\begin{aligned}\bar{R}_{ij} = &-\frac{1}{2}\bar{\gamma}^{kl}(\partial_k\partial_l\bar{\gamma}_{ij} + \partial_i\partial_j\bar{\gamma}_{kl} - \partial_k\partial_i\bar{\gamma}_{lj} - \partial_l\partial_j\bar{\gamma}_{ki}) \\ &+ \bar{\gamma}^{kl}\left[\bar{\Gamma}^m_{il}\bar{\Gamma}_{mkj} - \bar{\Gamma}^m_{ij}\bar{\Gamma}_{mkl}\right],\end{aligned} \tag{93}$$

where I denoted $\bar{\Gamma}_{ijk} = \bar{\gamma}_{il}\bar{\Gamma}^l_{jk}$ for compactness. Note that the last two terms are not the same as the usual two quadratic terms of the Ricci tensor. The first of the second derivative terms is just the Laplacian $\bar{\gamma}^{kl}\partial_k\partial_l\bar{\gamma}_{ij}$, and it doesn't cause any problems. However, the other second derivative terms cause major numerical issues [18, 19].

In BSSN-formalism the method of dealing with the issues is to rewrite these terms using auxiliary fields which are then evolved using their own evolution equations. I define

$$\bar{\Gamma}^i := \bar{\gamma}^{kl}\bar{\Gamma}^i_{kl}. \tag{94}$$

This can be rewritten in another form using metric compatibility

$$0 = \bar{D}_k\bar{\gamma}^{ki} = \partial_k\bar{\gamma}^{ki} + \bar{\Gamma}^k_{kl}\bar{\gamma}^{li} + \bar{\Gamma}^i_{kl}\bar{\gamma}^{lk}. \tag{95}$$

The middle term vanishes as

$$\bar{\Gamma}^k_{ki} = \partial_i \ln\sqrt{|\bar{\gamma}|} \tag{96}$$

and the determinant of the scaled metric is unity [10]. The two remaining terms give the relation

$$\bar{\Gamma}^i = -\partial_k\bar{\gamma}^{ki}, \tag{97}$$

which acts as an additional constraint equation.

The second derivatives in the Ricci tensor should be related to the derivatives of the auxiliary fields, as they arise from differentiating the Christoffel symbols. This indeed turns out to be the case, as the first partial derivatives of $\bar{\Gamma}^k$ satisfy the equation

$$\begin{aligned}\bar{\gamma}_{ki}\partial_j\bar{\Gamma}^k = &\bar{\gamma}^{mn}\left[\partial_j\partial_m\bar{\gamma}_{ni} - \frac{1}{2}\partial_i\partial_j\bar{\gamma}_{mn}\right] + \bar{\Gamma}_{imn}(\partial_j\bar{\gamma}^{mn}) \\ &+ \bar{\gamma}^{ml}\bar{\gamma}^{nk}\left[(\partial_j\bar{\gamma}_{ik})\bar{\Gamma}_{nml} + (\partial_j\bar{\gamma}_{nl})\bar{\Gamma}_{imk}\right].\end{aligned} \tag{98}$$

Comparing the first brackets with equation 93 suggests that the troublesome second derivatives can be eliminated with a term $\bar{\gamma}_{k(i}\partial_{j)}\bar{\Gamma}^k$. After some effort one finds that

$$-\frac{1}{2}\bar{\gamma}^{kl}(\partial_i\partial_j\bar{\gamma}_{kl} - \partial_k\partial_i\bar{\gamma}_{lj} - \partial_l\partial_j\bar{\gamma}_{ki}) = \bar{\gamma}_{k(i}\partial_{j)}\bar{\Gamma}^k + \bar{\gamma}^{ml}\bar{\Gamma}^n_{ij}\bar{\Gamma}_{nml} + \bar{\Gamma}^k\bar{\Gamma}_{(ij)k} + \frac{1}{2}\bar{\gamma}^{ml}\bar{\gamma}^{nk}\left[(\partial_j\bar{\gamma}_{nl})\bar{\Gamma}_{imk} + (\partial_i\bar{\gamma}_{nl})\bar{\Gamma}_{jmk}\right], \quad (99)$$

and substituting this into equation 93 results finally in

$$\bar{R}_{ij} = -\frac{1}{2}\bar{\gamma}^{kl}\partial_k\partial_l\bar{\gamma}_{ij} + \bar{\gamma}_{k(i}\partial_{j)}\bar{\Gamma}^k + \bar{\Gamma}^k\bar{\Gamma}_{(ij)k} + \bar{\gamma}^{kl}(2\bar{\Gamma}^m_{l(i}\bar{\Gamma}_{j)mk} + \bar{\Gamma}^m_{il}\bar{\Gamma}_{mkj}). \quad (100)$$

All of the second derivatives apart from the Laplacian term are now absorbed into the derivatives of $\bar{\Gamma}^k$.

Now with the Ricci tensor in a more numerically stable form, what remains is to write the evolution and constraint equations for the new set of dynamical fields ϕ, $\bar{\gamma}_{ij}$, K, $\bar{A}_{ij}$ and $\bar{\Gamma}^i$. For the sake of generality, I will keep the lapse function α and shift β in the equations for the moment.

I will start with the scalar quantities ϕ and K. Since the spatial metric is invertible by definition, the Jacobi formula states that

$$\partial_t\gamma = \gamma\gamma^{ik}\dot{\gamma}_{ki} \quad (101)$$

and substituting in equation 60 for $\dot{\gamma}_{ij}$ leaves

$$\partial_t\gamma = -2\alpha\gamma K + 2\gamma D_i\beta^i. \quad (102)$$

This form simplifies somewhat by writing the full spatial covariant derivative in terms of the BSSN-variables:

$$D_i\beta^i = \partial_i\beta^i + \Gamma^i_{ik}\beta^k = \partial_i\beta^i + \frac{1}{2\gamma}\partial_k\gamma. \quad (103)$$

Noting that $\gamma = e^{12\phi}$ and cancelling the overall factor of γ gives the evolution equation for the conformal factor,

$$\partial_t\phi = -\frac{1}{6}\alpha K + \frac{1}{6}\partial_i\beta^i + \beta^k\partial_k\phi. \quad (104)$$

The evolution of K is simpler to obtain, as it is sufficient to rewrite the term $K_{ij}K^{ij}$

in equation 64. The resulting equation is

$$\partial_t K = -D^2\alpha + \alpha(\bar{A}_{ij}\bar{A}^{ij} + \frac{1}{3}K^2) + 4\pi\alpha(\tilde{\rho} + S) + \beta^i\partial_i K. \tag{105}$$

With ϕ accounted for, the evolution equation for $\bar{\gamma}_{ij}$ can now be obtained from equation 60 by substituting in the expression for $\dot{\phi}$:

$$\partial_t\bar{\gamma}_{ij} = -2\alpha\bar{A}_{ij} - \frac{2}{3}\bar{\gamma}_{ij}\partial_k\beta^k - 4\bar{\gamma}_{ij}\beta^k\partial_k\phi + e^{-4\phi}(D_i\beta_j + D_j\beta_i). \tag{106}$$

By expanding the covariant derivatives in terms of the BSSN variables and raising the indices on β_i, the equation becomes

$$\partial_t\bar{\gamma}_{ij} = -2\alpha\bar{A}_{ij} - \frac{2}{3}\bar{\gamma}_{ij}\partial_k\beta^k + \beta^k\partial_k\bar{\gamma}_{ij} + \bar{\gamma}_{ik}\partial_j\beta^k + \bar{\gamma}_{jk}\partial_i\beta^k, \tag{107}$$

which is somewhat simpler to implement numerically. The evolution of $\bar{A}_{ij}$ is found in a similar way from equation 61 by subtracting its trace, resulting eventually in

$$\begin{aligned}\partial_t\bar{A}_{ij} = e^{-4\phi}\left((-D_iD_j\alpha)^{TF} + \alpha(R_{ij}^{TF} - 8\pi S_{ij}^{TF})\right) + \alpha(K\bar{A}_{ij} - 2\bar{A}_{ik}\bar{A}^k{}_j)\\ + \beta^k\partial_k\bar{A}_{ij} + \bar{A}_{ik}\partial_j\beta^k + \bar{A}_{jk}\partial_i\beta^k - \frac{2}{3}\bar{A}_{ij}\partial_k\beta^k.\end{aligned} \tag{108}$$

Here

$$R_{ij}^{TF} = R_{ij} - \frac{1}{3}\gamma_{ij}R \tag{109}$$

$$S_{ij}^{TF} = S_{ij} - \frac{1}{3}\gamma_{ij}S \tag{110}$$

$$(D_iD_j\alpha)^{TF} = D_iD_j\alpha - \frac{1}{3}\gamma_{ij}\gamma^{kl}D_kD_l\alpha \tag{111}$$

are the trace-free parts of the tensors.

The last remaining equations necessary are the evolution equations for the auxiliary fields $\bar{\Gamma}^i$. These equations are relatively simple to obtain by differentiating both sides of equation 97 and substituting in the time derivative of the conformally related metric. This results in

$$\partial_t\bar{\Gamma}^i = -\partial_j(2\alpha\bar{A}^{ij} - 2\bar{\gamma}^{k(j}\partial_k\beta^{i)} + \frac{2}{3}\bar{\gamma}^{ij}\partial_k\beta^k + \beta^k\partial_k\bar{\gamma}^{ij}). \tag{112}$$

However, it turns out that the divergence $\partial_j\bar{A}^{ij}$ causes numerical issues that can be solved by eliminating it using the momentum constraint [19]. Note first that $D_j A^{ij} = e^{-10\phi}\bar{D}_j(e^{6\phi}\bar{A}^{ij})$, which can be verified by a brief calculation. With this substitution the momentum constraint becomes

$$\bar{D}_j\bar{A}^{ij} = -6\bar{A}^{ij}\partial_j\phi + \frac{2}{3}\bar{\gamma}^{ij}\partial_j K + 8\pi\bar{\gamma}^{ij}S_j. \tag{113}$$

After solving for $\partial_j\bar{A}^{ij}$ and plugging it into equation 112, the evolution equation is finally

$$\begin{aligned}\partial_t\bar{\Gamma}^i = {} & -\bar{A}^{ij}\partial_j\alpha + 2\alpha\left(\bar{\Gamma}^i_{jk}\bar{A}^{kj} - \frac{2}{3}\bar{\gamma}^{ij}\partial_j K - 8\pi\bar{\gamma}^{ij}S_j + 6\bar{A}^{ij}\partial_j\phi\right) \\ & + \beta^j\partial_j\bar{\Gamma}^i - \bar{\Gamma}^j\partial_j\beta^i + \frac{2}{3}\bar{\Gamma}^i\partial_j\beta^j + \frac{1}{3}\bar{\gamma}^{ki}\partial_k\partial_j\beta^j + \bar{\gamma}^{kj}\partial_k\partial_j\beta^i.\end{aligned} \tag{114}$$

As the last thing, I need to rewrite the Hamiltonian constraint equation using the new set of variables. Splitting the trace away from the extrinsic curvature leaves the constraint equation as

$$R - \bar{A}_{ij}\bar{A}^{ij} + \frac{2}{3}K^2 = 16\pi\tilde{\rho}. \tag{115}$$

While this is the form of the constraint equation most convenient to implement numerically, in the next section another form will prove useful. Noting that

$$e^{5\phi}\gamma^{ij}\left[\bar{D}_i\bar{D}_j\phi + (\bar{D}_i\phi)(\bar{D}_j\phi)\right] = \bar{\gamma}^{ij}\bar{D}_i\bar{D}_j e^{\phi} \tag{116}$$

and substituting equations 92 and 116 into the Hamiltonian constraint results in

$$\bar{\gamma}^{ij}\bar{D}_i\bar{D}_j e^{\phi} - \frac{e^{\phi}}{8}\bar{R} + \frac{e^{5\phi}}{8}\bar{A}_{ij}\bar{A}^{ij} - \frac{e^{5\phi}}{12}K^2 = -2\pi e^{5\phi}\tilde{\rho}. \tag{117}$$

Equations 104, 105, 107, 108 and 114 together constitute the BSSN-equations, and they are equivalent to the ADM-system of equations [18]. As is the case with the ADM-formalism, the continuity equation is still needed to close the system and the Hamiltonian and momentum constraints should be fulfilled on each timeslice. Introducing the auxiliary fields $\bar{\Gamma}^i$ added one more constraint in equation 97, and in addition splitting off the conformal factor also requires $\bar{\gamma} = 1$, which acts as another constraint. In principle these relations could be used to solve some of the variables instead of evolving them freely.

As with the ADM-formalism, I choose the synchronous gauge with zero shift. In the synchronous gauge choosing zero initial velocity ensures that the velocity is always zero and the velocity can then be dropped from the equations. With these choices the evolution equations for the BSSN-variables along with the continuity equation reduce into

$$\begin{aligned}
\partial_t\phi &= -\frac{1}{6}K && (118)\\
\partial_t K &= \bar{A}_{ij}\bar{A}^{ij} + \frac{1}{3}K^2 + 4\pi\rho && (119)\\
\partial_t\bar{\gamma}_{ij} &= -2\bar{A}_{ij} && (120)\\
\partial_t\bar{A}_{ij} &= e^{-4\phi}R^{TF}_{ij} + K\bar{A}_{ij} - 2\bar{A}_{ik}\bar{A}^{k}{}_{j} && (121)\\
\partial_t\bar{\Gamma}^i &= 2\bar{\Gamma}^i_{jk}\bar{A}^{kj} - \frac{4}{3}\bar{\gamma}^{ij}\partial_j K + 12\bar{A}^{ij}\partial_j\phi && (122)\\
\dot{\rho} &= K\rho. && (123)
\end{aligned}$$

4.2 BSSN-equations for perturbations

As was the case with the ADM-equations, the numerical error at the early times will be prohibitively large if this system is evolved directly without subtracting the background quantities analytically. Luckily, this turns out to be somewhat simpler in BSSN-formalism due to the conformal transverse-traceless split.

I denote[5] $\phi = \phi_0 + \delta\phi$, $K = K_0(1+\delta_K)$ and $\rho = \rho_0(1+\delta)$. As the background spatial metric is just $a^2\delta_{ij}$, it is natural to split $\bar{\gamma}_{ij} = \delta_{ij} + h_{ij}$ and so the spatial metric becomes

$$\gamma_{ij} = e^{4\phi_0}\delta_{ij} + e^{4\phi_0}(e^{4\delta\phi} - 1)\delta_{ij} + e^{4(\phi_0+\delta\phi)}h_{ij}. \tag{124}$$

The first term is the only one zeroth order in the perturbation and I can identify

$$\phi_0 = \frac{1}{2}\ln a. \tag{125}$$

The split in the trace K was already discussed in the ADM case and so

$$K_0 = -\frac{3\dot{a}}{a} \tag{126}$$

---

[5] In the context of the BSSN-formalism I will use the subscript 0 for the background quantities so that there is no confusion with the conformally related tensors.

as before. Writing the extrinsic curvature in terms of the split quantities gives

$$\begin{aligned} K_{ij} = -a\dot{a}\Big(&\delta_{ij} + (e^{4\delta\phi} - 1)\delta_{ij} + e^{4\delta\phi}\delta_K\delta_{ij} \\ &+ e^{4\delta\phi}(1+\delta_K)h_{ij} - \frac{a}{\dot{a}}e^{4\delta\phi}\bar{A}_{ij}\Big). \end{aligned} \tag{127}$$

The entire background is accounted for in the first term and, so the traceless part $\bar{A}_{ij}$ must be entirely perturbation. The last variables to consider are $\bar{\Gamma}^i$. However, as the background metric is a constant in space, the background auxiliary fields must be zero by equation 97. Then, $\bar{\Gamma}^i$ must be purely perturbation as well.

I can now plug in the background split into the BSSN-equations with synchronous gauge and zero peculiar velocity. All terms in equations 113, 120, 121 and 122 are already proportional to the perturbation and so it is not necessary to subtract the background. In the rest of the equations the background terms cancel due to the Friedmann equations, leaving

$$\partial_t \delta\phi = \frac{1}{2}\frac{\dot{a}}{a}\delta_K \tag{128}$$

$$\partial_t \delta_K = -\frac{a}{3\dot{a}}(\delta^{ik} + \tilde{h}^{ik})(\delta^{jl} + \tilde{h}^{jl})\bar{A}_{ij}\bar{A}_{kl} - \frac{1}{2}\frac{\dot{a}}{a}\delta_K - \frac{\dot{a}}{a}\delta_K^2 - \frac{1}{2}\frac{\dot{a}}{a}\delta \tag{129}$$

$$\partial_t h_{ij} = -2\bar{A}_{ij} \tag{130}$$

$$\partial_t \bar{A}_{ij} = e^{-4\phi}R^{TF}_{ij} - \frac{3\dot{a}}{a}(1+\delta_K)\bar{A}_{ij} - 2(\delta^{kl} + \tilde{h}^{kl})\bar{A}_{ik}\bar{A}_{lj} \tag{131}$$

$$\begin{aligned} \partial_t \bar{\Gamma}^i = {}& 2\bar{\Gamma}^i_{jk}(\delta^{kl} + \tilde{h}^{kl})(\delta^{jn} + \tilde{h}^{jn})\bar{A}_{ln} + \frac{4\dot{a}}{a}(\delta^{ij} + \tilde{h}^{ij})\partial_j\delta_K \\ &+ 12(\delta^{il} + \tilde{h}^{il})(\delta^{jn} + \tilde{h}^{jn})\bar{A}_{ln}\partial_j\phi \end{aligned} \tag{132}$$

$$\partial_t \delta = -\frac{3\dot{a}}{a}(\delta_K + \delta\delta_K). \tag{133}$$

$$R - (\delta^{ik} + \tilde{h}^{ik})(\delta^{jl} + \tilde{h}^{jl})\bar{A}_{ij}\bar{A}_{kl} + \frac{6\dot{a}^2}{a^2}(2\delta_K + \delta_K^2) = \frac{6\dot{a}^2}{a^2}\delta \tag{134}$$

$$(\delta^{jk} + \tilde{h}^{jk})\bar{D}_j\bar{A}_{ik} + 6(\delta^{jk} + \tilde{h}^{jk})\bar{A}_{ik}\partial_j\delta\phi + \frac{2\dot{a}}{a}\partial_i\delta_K = 0 \tag{135}$$

In order to preserve numerical accuracy, the perturbation of the inverse conformally related metric $\tilde{h}^{ij}$ should be calculated in an analogous way to equation 82.

5 Initial conditions

In the previous two sections, I discussed two different sets of equations for evolving a spacetime starting from some initial configuration. However, constructing this initial configuration is a somewhat more subtle problem than one might imagine. In this subsection, I will construct the initial data I will be using by adopting a simplifying assumption from [23]. The reader should consult [18] for a more general discussion.

5.1 Solving the constraint equations

As is the case on any other timeslice as well, the initial data is constrained by the Hamiltonian and momentum constraint equations. One could expect that the matter of solving the initial conditions amount to simply solving the constraint equations for the given initial energy density and velocity configuration. However, counting the available degrees of freedom reveals that there is more to the problem. The degrees of freedom are the simplest to count in the ADM-formalism. The variables to specify are the initial spatial metric and extrinsic curvature, both of which have six independent components. There are then twelve degrees of freedom to specify in the initial data, whereas there are only four constraint equations.

This is not too surprising: In general relativity there is always the freedom to choose the coordinate system as one sees fit. Specifying the spatial coordinates on the initial timeslice takes three degrees of freedom, while specifying the initial time takes one more. This leaves four degrees of freedom, which correspond with the two modes of gravitational radiation [18].

While all degrees of freedom are now accounted for, actually specifying how these degrees of freedom correspond with the variables at hand is more difficult. It turns out to be easiest to start from the conformal transformation of the BSSN-formalism. Adopting the notation again from [18], I will denote $\psi \equiv e^{\phi}$. With this notation the constraint equations read

$$\bar{D}^i \bar{D}_i \psi - \frac{1}{8}\psi \bar{R} + \frac{1}{8}\psi^5 \bar{A}_{ij}\bar{A}^{ij} - \frac{1}{12}\psi^5 K^2 = -2\pi\psi^5\rho \tag{136}$$

and

$$\bar{D}_j(\psi^6 \bar{A}^{ij}) - \frac{2}{3}\psi^6 \bar{D}^i K = 8\pi\psi^6 S^i. \tag{137}$$

For given ρ and S^i these equations serve to determine the conformal factor ψ and the divergence of $\bar{A}_{ij}$. This leaves K, $\bar{\gamma}_{ij}$ and the transverse, or divergence free, part of $\bar{A}_{ij}$ to be freely specified.

These last variables specify the gauge and the initial gravitational wave content, although the exact way depends on the initial conditions in question. It is common to associate K with the choice of time coordinate and the transverse part of $\bar{A}_{ij}$ with the gravitational radiation [18].

While this issue is of great importance when discussing, say, initial conditions for black holes, the physical situation in my case makes the problem somewhat simpler. I want to consider a FLRW-background with a small initial perturbation. The initial choices for variables should then reduce to their FLRW-values in the limit of vanishing perturbation. The FLRW-initial values have a flat spatial metric with a constant K and zero $\bar{A}_{ij}$.

Following [23], I demand that the initial spatial metric is conformally flat, $\bar{\gamma}_{ij} = \delta_{ij}$. For the rest of the variables, I require that they take their FLRW values with constant K and vanishing $\bar{A}_{ij}$ [23]. Moving into the synchronous gauge and requiring zero initial peculiar velocity, the momentum constraint reduces into

$$\bar{D}_j(\psi^6 \bar{A}^{ij}) = 0, \tag{138}$$

which is clearly satisfied by the choice $\bar{A}_{ij} = 0$.

In turn, the Hamiltonian constraint with the above choices at the initial slice becomes [23]

$$\nabla^2\psi = \left(\frac{1}{12}K^2 - 2\pi\rho\right)\psi^5. \tag{139}$$

Substituting in $K = -3\dot{a}/a$ into the Hamiltonian constraint, writing $\rho = \rho_0(1+\delta)$ and cancelling the background terms using the Friedmann equations results in

$$\nabla^2\psi = -\frac{3}{4}\frac{\dot{a}^2}{a^2}\delta\psi^5. \tag{140}$$

Denoting

$$f(\vec{x}) = -\frac{3}{4}\frac{\dot{a}^2}{a^2}\delta(\vec{x}), \tag{141}$$

where all quantities are evaluated at the initial timeslice, brings the equation to the simple form

$$\nabla^2\psi = f(\vec{x})\psi^5. \tag{142}$$

Despite its simplicity, equation 142 is rather difficult to solve exactly. It is possible to solve the equation numerically, although specific methods have to be utilised in order to have the solution converge [49]. However, there is some simplification that can be gained by noting that the function f is proportional to the density perturbation.

In order to make this more apparent, I write the initial density perturbation as $\delta(\vec{x}) = \delta_0\tilde{\delta}(\vec{x})$, where the values of $\tilde{\delta}$ are of order unity. Similarly, I can then denote $f = \delta_0\tilde{f}$. In the case of a vanishing perturbation, ψ should reduce to its FLRW value of $\psi = \sqrt{a}$, and so ψ should have the form

$$\psi = \sqrt{a}(1 + \delta_0\psi_1), \tag{143}$$

where ψ_1 is some unknown function. Substituting this into equation 142 results in

$$\nabla^2\psi_1 = a^2\tilde{f}(1 + \delta_0\psi_1)^5 = a^2\tilde{f} + 5a^2\delta_0\tilde{f}\psi_1 + \mathcal{O}(\delta_0^2). \tag{144}$$

In principle, one could iterate this procedure to solve ψ to the desired order of accuracy.

However, this approach is not without its issues. To first order in δ_0, the Hamiltonian constraint reduces into a simple Poisson equation. By expanding the conformal factor in powers of δ_0,

$$\psi = \sqrt{a}(1 + \delta_0\psi_1 + \delta_0^2\psi_2 + ...) \tag{145}$$

the constraint equation 142 becomes

$$\delta_0\left[\nabla^2\psi_1 - a^2\tilde{f}\right] + \delta_0^2\left[\nabla^2\psi_2 - 5a^2\tilde{f}\psi_1\right] + ... = 0. \tag{146}$$

Requiring each of the coefficients to vanish results in the set of Poisson equations

$$\begin{cases} \nabla^2\psi_1 = a^2\tilde{f} \\ \nabla^2\psi_2 = 5a^2\tilde{f}\psi_1 \\ \nabla^2\psi_3 = ... \end{cases} . \tag{147}$$

As the source term of each equation depends only on the solution to the equations above it, this system can be solved starting from the first equation.

However, for certain initial data and boundary conditions the system of equations does not have any solutions. A simple example of this in one dimension is a sinusoidal initial perturbation with periodic boundary conditions,

$$f \propto \sin(2\pi x/L), \tag{148}$$

and the domain $[0,L]$. The solution to the first equation is clearly also sinusoidal, $\psi_1 \propto \sin(2\pi x/L)$, and so the second equation is

$$\partial_x^2\psi_2 \propto \sin^2(2\pi x/L). \tag{149}$$

This equation has no solutions satisfying the periodic boundary conditions. This can be seen by integrating both sides of the equation over the entire domain. The integral of the left hand side is

$$\int_0^L \partial_x^2\psi_2 dx = \partial_x\psi_2(L) - \partial_x\psi_2(0) = 0, \tag{150}$$

where the derivatives cancel due to the periodicity. This is in contrast with the right hand side, which has the same sign everywhere, and therefore its integral cannot vanish. This same approach generalizes to higher dimensions as well.

Whether or not this is an indication of a deeper problem is not clear at this point. It is possible that the issue is due to the expansion procedure and could be avoided with a different expansion scheme. The original equation 142 can be solved numerically even for the sinusoidal initial perturbation of the example [49], which lends credibility for this claim. For the current purposes, I will settle to solving the constraint equation to first order, but further research is necessary on this topic.

These problems withstanding, after solving for ϕ from equation 139 the rest of the initial conditions are simple, particularly in the BSSN-formalism. The conformal factor perturbation $\delta\phi$ can be solved from

$$e^{\delta\phi} = 1 + \delta_0 \psi_1 \tag{151}$$

to the desired accuracy and the rest of the initial conditions were chosen to be $h_{ij} = \bar{A}_{ij} = \delta_K = 0$. As the initial spatial metric is conformally flat, the auxiliary functions must be $\bar{\Gamma}^i = 0$ at the initial time as well.

The ADM initial conditions can then be constructed using the BSSN variables. Comparing the definitions for the split spatial metric in the two formalisms shows that the perturbation of the spatial metric is

$$\delta\gamma_{ij} = (e^{4\delta\phi} - 1)\delta_{ij} + e^{4\delta\phi} h_{ij} = 4\delta\phi\delta_{ij} + \mathcal{O}(\delta_0^2). \tag{152}$$

The perturbation of K_{ij} in terms of the BSSN-variables was already calculated in equation 127 and plugging in the BSSN-initial conditions results in

$$\delta K_{ij} = (e^{4\delta\phi} - 1)\delta_{ij} = 4\delta\phi\delta_{ij} + \mathcal{O}(\delta_0^2). \tag{153}$$

5.2 The initial density perturbation

In this thesis, I will consider two different initial density configurations. The first of these is a sinusoidal density perturbation which will be used for testing purposes and comparisons with existing literature. The second configuration is a cubic lattice with overdensities at the edges of the cube, as mentioned in the introduction. For both initial conditions I will impose periodic boundary conditions. I will also choose $a = 1$ at the initial time for simplicity.

I will start with the simpler sinusoidal configuration. The density profile is

$$\delta_s(\vec{x}) = \delta_0 \left[\sin(2\pi x/L) + \sin(2\pi y/L) + \sin(2\pi z/L)\right], \tag{154}$$

where δ_0 is the initial amplitude of the perturbation and L is the comoving length of the computation lattice. The main advantage of this configuration is that to first order in δ_0 the constraint equations are particularly easy to solve on the initial timeslice. Equation 142 reduces into

$$\nabla^2\psi_1 = \sum_i \sin(2\pi x^i/L) + \mathcal{O}(\delta_0), \tag{155}$$

and the solution for ψ is

$$\psi(\vec{x}) = 1 + \delta_0 \frac{L^2}{4\pi^2} \sum_i \sin(2\pi x^i/L) + \mathcal{O}(\delta_0^2). \tag{156}$$

It must be noted that these initial conditions are subject to the problems discussed in the previous section. However, the sinusoidal solution is visually close to the numerical solution depicted in [49]. The resulting violation of the Hamiltonian constraint will be discussed in more detail in chapter 8.

The second density configuration is chosen to emulate an arrangement of filaments in the early universe. The actual universe has structure on multiple different scales and no easily usable symmetries. I will settle for a toy model in which I require again a cubic lattice symmetry and the filaments follow the edges of a lattice box.

A simple choice for the cross section of a filament is the Gaussian

$$g(x,y) = \exp(-(x^2+y^2)/\sigma^2), \tag{157}$$

where σ is the width parameter of the filament. Filaments can be placed at each edge of the box $[0,L]^3$ with the sum

$$\begin{aligned} F(x,y,z) = {} & g(x,y) + g(x-L,y) + g(x,y-L) + g(x-L,y-L) \\ & + g(x,z) + g(x-L,z) + g(x,z-L) + g(x-L,z-L) \\ & + g(y,z) + g(y-L,z) + g(y,z-L) + g(y-L,z-L). \end{aligned} \tag{158}$$

In this configuration the different filaments overlap at the vertices of the box and so the value of F at each vertex is triple the typical value on each edge. As such, it is useful to regulate F with a function that saturates to some value. I define the final density profile as

$$\delta_f(\vec{x}) = \delta_0(\tanh(F(\vec{x})) - p), \tag{159}$$

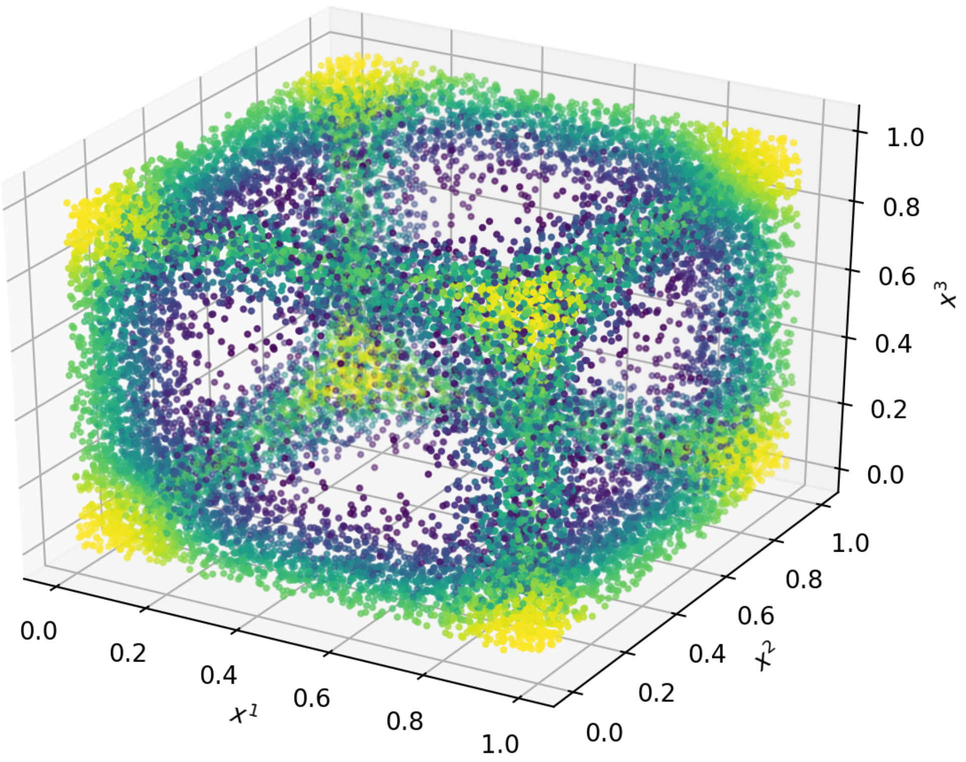

Figure 2. The three-dimensional density perturbation δ_f as defined in equation 159. The color of each marker represents the density perturbation at the point and the side of the box was chosen $L = 1$.

where the parameter p is chosen such that

$$\int_{\text{Box}} d^3x \delta_f(\vec{x}) = 0. \tag{160}$$

The resulting density perturbation is depicted in figure 2.

For each of these initial conditions, I will employ periodic boundary conditions. The main advantage to this assumption is that the metric of the entire timeslice can be determined by simulating just one lattice box. This will turn out to be useful in particular when analyzing light propagation in the resulting spacetimes.

5.3 The length scale of the initial conditions

A last thing to note is the length scale of the initial conditions. In the numerical implementation, it is convenient to use units of length l_u in which the physical length of the computation box on the initial timeslice is $L = 1\ l_u$. Similarly, I will use a units of time t_u in which the initial time is $t_{init} = b^{-1}\ t_u$ for some dimensionless parameter b. I will refer to this unit system as the code units. As I have set $c = 1$ in code units, the physical units of length and time must be related by $l_u = ct_u$. The units of length and time never explicitly enter the ADM- and BSSN-equations, and they are only used in interpreting the results. Thus, one simulation can correspond to multiple physical situations with different length scales and initial times.

In this text, I will assume that the initial time corresponds to the cosmic microwave background. The Hubble rate at the CMB can be expressed using equation 14 as

$$H_{CMB} = H_0(1 + z_{CMB})^{3/2}, \tag{161}$$

where $z_{CMB} \approx 1100$ is the redshift at the CMB and $H_0 \approx 70\,\mathrm{km/s/Mpc}$ is the current Hubble rate [4]. The initial time can then be solved from equation 14 as

$$t_{init} = \frac{2}{3H_{CMB}} = \frac{2}{3(1 + z_{CMB})^{3/2}H_0} \approx 80\,\mathrm{kpc/c}, \tag{162}$$

where $c \approx 3.0 \cdot 10^5$ km/s is the speed of light in physical units [4]. The units of time in the numerical implementation must then be $t_u \approx b \cdot 80\,\mathrm{kpc/c}$, and the units of length are $l_u \approx b^{-1} \cdot 80\,\mathrm{kpc}$.

The comoving length scale of a structure is now the physical length of the box measured on the present timeslice [4]. Denoting the current scale factor as a_0, the comoving length of the box L_{cm} is

$$L_{cm} = \frac{a_0}{a_{CMB}} L = (1 + z_{CMB})L \approx b \cdot 90\,\mathrm{Mpc}. \tag{163}$$

The initial time parameter b corresponding to a given comoving length scale is then simply

$$b = \frac{L_{cm}}{90\,\mathrm{Mpc}}. \tag{164}$$

From now on I will not explicitly write out the code units l_u and t_u. Instead, I will treat the length and time coordinates as if they were dimensionless.

6 Light propagation

As I noted in the introduction, the spacetime metric itself is not an observable quantity. Instead, comparisons between the simulations and observations must be done on the ways the curvature affects the motion of the matter and the radiation in the universe. The focus of this thesis is on the latter, and I will discuss how to calculate the trajectory and the redshift of a light ray in this section. I will discuss both of these in the context of a FLRW-universe and in the inhomogeneous case.

6.1 The geodesic equation

From elementary optics we know that rays of light in vacuum propagate along straight lines. However, generalizing the notion of a straight line to a curved spacetime is not entirely straightforward. One defining property of a straight line in a flat space is that it minimizes the distance between its endpoints. Mimicking this, the notion of a geodesic can be defined as a path which is an extremum of the space-time interval

$$l[x^\mu(u)] = \int ds = \int du \sqrt{g_{\mu\nu}\frac{dx^\mu}{du}\frac{dx^\nu}{du}}, \tag{165}$$

where the integral is calculated along the path $x(u)$ in question.

In general relativity, freely falling objects move along geodesics by assumption. Denoting $k^\mu = dx^\mu/du$, it can be proven that the geodesics are found as solutions to the geodesic equation [27]

$$k^\nu \nabla_\nu k^\mu = 0, \tag{166}$$

or equivalently

$$\frac{d^2x^\mu}{du^2} + \Gamma^\mu_{\nu\rho}\frac{dx^\nu}{du}\frac{dx^\rho}{du} = 0. \tag{167}$$

Note that these equations are sensitive to the parametrization of the geodesic. The curve parameter u satisfying the above equations is called the affine parameter. While equation 167 is assumed for point particles, it is also valid for radiation whose wavelength is much smaller than the scale of the curvature[6] [9]. Given this assumption, radiation moves along null geodesics whose velocity vectors satisfy

$$k_\mu k^\mu = 0. \tag{168}$$

This relation is often written as $ds^2 = 0$ along null geodesics.

The solutions for the geodesic equation can be found easily in the homogeneous case. Consider the FLRW-metric in the form of equation 8. A radial trajectory with $d\theta = 0 = d\phi$ satisfies the null condition $ds^2 = 0$ if

$$dt = \pm a(1 - kr^2)^{-1/2} dr. \tag{169}$$

This relation can be integrated to find

$$\int_{t_1}^{t_2} \frac{dt}{a(t)} = \pm \int_{r_1}^{r^2} \frac{dr}{\sqrt{1 - kr^2}} = \pm(\chi(r_2) - \chi(r_1)), \tag{170}$$

where the form of $\chi(r)$ depends on the curvature:

$$\chi(r) = \begin{cases} \frac{1}{\sqrt{k}} \sin(\sqrt{k} r), & k > 0 \\ r, & k = 0 \\ \frac{1}{\sqrt{-k}} \sinh(\sqrt{-k} r), & k < 0 \end{cases} . \tag{171}$$

The coordinate system can always be chosen so that the geodesic starts at the origin, so the above equations actually describe general null geodesics in a FLRW-universe.

In the inhomogeneous case, it is usually necessary to solve the geodesic equation numerically. Following the approach in [50], the solver is easiest to implement starting from the form in equation 166. I will consider metrics of the form

$$ds^2 = -\alpha^2 dt^2 + \gamma_{ij} dx^i dx^j. \tag{172}$$

Using metric compatibility the geodesic equation becomes

$$0 = g^{\mu\alpha} k^\nu \nabla_\nu k_\alpha, \tag{173}$$

---

[6] This assumption is called the geometrical optics approximation.

which is only satisfied if

$$k^\nu \nabla_\nu k_\alpha = k^\nu \partial_\nu k_\alpha - \Gamma^\beta_{\nu\alpha} k_\beta k^\nu = 0. \tag{174}$$

Note that here $\Gamma^\mu_{\nu\alpha}$ is the full four-dimensional Christoffel symbol. The first term is clearly just the derivative of k_α along the geodesic. The second term on the other hand is

$$\Gamma^\beta_{\nu\alpha} k_\beta k^\nu = \Gamma_{\beta\alpha\nu} k^\beta k^\alpha = \frac{1}{2} k^\alpha k^\beta \partial_\nu g_{\alpha\beta}. \tag{175}$$

and so the geodesic equation becomes

$$\frac{dk_\mu}{du} = -\frac{1}{2}(k^0)^2 \partial_\mu(\alpha^2) + \frac{1}{2} k^i k^j \partial_\mu \gamma_{ij}. \tag{176}$$

This equation can be simplified somewhat by noting that

$$k^0 = \frac{dt}{du} \tag{177}$$

along the curve by definition. The derivatives along the curve can then be exchanged for time derivatives, resulting in

$$\frac{dk_\mu}{dt} = -k^0 \alpha \partial_\mu \alpha + \frac{1}{2}(k^0)^{-1} k^i k^j \partial_\mu \gamma_{ij}, \tag{178}$$

where the zeroth component k^0 should be solved from the normalization

$$0 = k^\mu k_\mu = -\alpha^2 (k^0)^2 + \gamma_{ij} k^i k^j. \tag{179}$$

Note that the geodesic equation preserves this normalization, since

$$\frac{d}{du}(k_\mu k^\mu) = k^\alpha \partial_\alpha (k_\mu k^\mu) = k^\alpha k_\mu k_\nu \partial_\alpha g^{\mu\nu} + 2 g^{\mu\nu} k_\nu \frac{dk_\mu}{du} \tag{180}$$

$$= -k^\alpha k^\mu k^\nu \partial_\alpha g_{\mu\nu} + g^{\mu\nu} k_\nu k^\alpha k^\beta \partial_\mu g_{\alpha\beta} = 0. \tag{181}$$

The evolution of k^0 can therefore be accounted for analytically.

In the end the geodesic equation can be expressed as the system

$$\frac{dx^i}{dt} = (k^0)^{-1}k^i \tag{182}$$

$$\frac{dk_i}{dt} = -k^0\alpha\partial_i\alpha + \frac{1}{2}(k^0)^{-1}k^k k^l \partial_i\gamma_{kl}. \tag{183}$$

In the absence of pathologies, in the metric this form of the geodesic equation is simple to solve numerically. As the equation is a second order ordinary differential equation, the initial conditions one needs are both the initial location in the spacetime and the initial 4-velocity vector of the trajectory. The latter is just the photon wave 4-vector. In the coordinate system comoving with the matter flow, its components are $k^\mu = \omega(1,\vec{k})$, where ω is the frequency of the radiation measured by a comoving observer at the source and $\vec{k}$ is the spatial wave vector. The normalization of the latter at the initial time is fixed by the null condition.

6.2 Redshift

Once the null geodesic has been calculated, finding the redshift along it is not complicated. The frequency of the observed photon is just the zero-component of its wave vector in the rest frame of the observer. Denoting the 4-velocity of the observer as u^μ_O, the observed frequency is then $\omega_O = u^\mu_O k^O_\mu$, where k^O_μ is evaluated at the observer. Similarly, the source frequency is $\omega_S = u^\mu_S k^S_\mu$. The redshift is then by definition the relative difference between the observer and source frequencies, [9]

$$z = \frac{\omega_S - \omega_O}{\omega_O} = \frac{u^\mu_S k^S_\mu}{u^\nu_O k^O_\nu} - 1. \tag{184}$$

For comoving sources and observers this simplifies even more into

$$z = \frac{k^0(t_S)}{k^0(t_O)} - 1, \tag{185}$$

as long as the photon trajectory is parametrized by the affine parameter. Note that any overall constant multiple of k^μ cancels in the geodesic equations 182 and 183. Thus, the redshift is independent of the initial frequency as a ratio of frequencies on the same geodesic.

It is simple to show that these formulas reduce into the familiar FLRW-results in the case $\gamma_{ij} = a^2(t)\delta_{ij}$. For a homogeneous metric, the covariant 3-momentum components k_i are constants and so

$$k^0(O) = \sqrt{a^{-2}(t_{obs})\delta^{ij}k_ik_j} = \frac{a(t_{em})}{a(t_{obs})}\sqrt{a^{-2}(t_{em})\delta^{ij}k_ik_j} = \frac{a(t_{em})}{a(t_{obs})}k^0(S), \qquad (186)$$

where t_{obs} and t_{em} are the times of observing and emitting the light ray respectively. Plugging this into the equation 185 results in

$$z = \frac{a(t_{obs})}{a(t_{em})} - 1, \qquad (187)$$

which is a relation found section 2.2 and in any textbook [27].

7 Numerical methods

Here, I will discuss the numerical implementation of the solver to the Einstein equations. I will first go through how to solve a system of hyperbolic partial differential equations using the method of lines. In order to do this, I will first briefly explain the method of finite differences for calculating numerical derivatives. After this, I will discuss relaxation methods for solving elliptic differential equations, and lastly I will give some additional details on the implementation of the simulation.

7.1 Finite differences

As any physical computer is capable of storing only a finite amount of data points, any numerical function must either be defined on a finite lattice or in terms of a finite number of basis functions. The limiting processes used in defining derivatives in mathematics are therefore impossible to reproduce perfectly, and we must settle for approximations. The most commonly used approximation is the finite differences. As the topic is discussed in any textbook on numerical methods [51], I will only give a rough overview of it.

It is illustrative to start with a simple example. Consider a function f with the Taylor expansion

$$f(x) = f(x_0) + f'(x_0)h + \frac{1}{2}f''(x_0)h^2 + \frac{1}{6}f'''(x)h^3 + \mathcal{O}(h^4), \tag{188}$$

where $h = x - x_0$. There are several different ways to solve the first derivative, the simplest of which are

$$f'(x) = \frac{f(x+h) - f(x)}{h} + \mathcal{O}(h^2). \tag{189}$$

$$f'(x) = \frac{f(x) - f(x-h)}{h} + \mathcal{O}(h^2) \tag{190}$$

$$f'(x) = \frac{f(x+h) - f(x-h)}{2h} + \mathcal{O}(h^3). \tag{191}$$

For a function defined on discrete points, the small number h is usually taken to be the grid spacing. Equations 189, 190 and 191 are called the forwards, backwards and central finite differences of the first derivative. Note also that in the central difference the second order terms vanish exactly and the derivative is accurate to third order in h.

A similar procedure can be extended to any derivative of any order of accuracy. Defining $f_n(x) = f(x + nh)$ for any integer n, the finite differences take the form

$$f^{(m)}(x) = \frac{1}{h^m} \sum_{n=-\infty}^{\infty} c_n f_n(x), \tag{192}$$

where c_n are the finite difference coefficients which can be found in tables [52]. Note also that the same formulas are applicable to partial derivatives with respect to a single variable as well.

A cursory inspection of the Einstein equation shows that I need approximations for only first and second derivatives. As the boundary conditions are periodic, I can use the central finite differences throughout the lattice instead of switching to a forwards or backwards difference at the boundary. Choosing fourth order accuracy results in the finite differences [52]

$$f' = \frac{1}{h}\left(-\frac{1}{12}f_2 + \frac{2}{3}f_1 - \frac{2}{3}f_{-1} + \frac{1}{12}f_{-2}\right) \tag{193}$$

$$f'' = \frac{1}{h^2}\left(-\frac{1}{12}f_2 + \frac{4}{3}f_1 - \frac{5}{2}f_0 + \frac{4}{3}f_1 - \frac{1}{12}f_2\right). \tag{194}$$

All that remains is to find approximations for the mixed second derivatives. Consider a function $f(x,y)$ and denote[7] $f_{nm}(x,y) = f(x + nh, y + mh)$. I also write $f^y = \partial_y f$ to avoid clutter. The mixed second derivative is then to fourth order

$$\partial_x \partial_y f = \frac{1}{h}\left(-\frac{1}{12}f^y_{20} + \frac{2}{3}f^y_{10} - \frac{2}{3}f^y_{-10} + \frac{1}{12}f^y_{-20}\right) + \mathcal{O}(h^4) \tag{195}$$

---

[7] Here, I assume that the grid spacing is identical in both directions.

and plugging in the finite difference for f^y gives the result

$$\begin{aligned}\partial_x\partial_y f = \frac{1}{h^2}\Big(&\frac{1}{144}f_{22} - \frac{1}{18}f_{21} + \frac{1}{18}f_{2-1} - \frac{1}{144}f_{2-2} \\ &- \frac{1}{18}f_{12} + \frac{4}{9}f_{11} - \frac{4}{9}f_{1-1} + \frac{1}{18}f_{1-2} \\ &+ \frac{1}{18}f_{-12} - \frac{4}{9}f_{-11} + \frac{4}{9}f_{-1-1} - \frac{1}{18}f_{-1-2} \\ &-\frac{1}{144}f_{-22} + \frac{1}{18}f_{-21} - \frac{1}{18}f_{-2-1} + \frac{1}{144}f_{-2-2}\Big) + \mathcal{O}(h^4). \qquad (196)\end{aligned}$$

7.2 Method of lines

While there are many different schemes for solving hyperbolic differential equations, I chose the method of lines for the problem. In this section, I will first describe the general procedure for the method following [18]. Afterwards, I will apply the method of lines to the simple example of the one-dimensional wave equation, as this will avoid the complications of the full Einstein equations.

In principle, the procedure of the method of lines is very simple. Consider a hyperbolic partial differential equation of the form

$$\frac{\partial y}{\partial t} = F(y,\partial_1 y,...), \qquad (197)$$

where $y = y(t,x^1,...,x^k)$ and F is a given function of y_i and its partial derivatives. I then discretize the domain in all but one direction into a $N_1 \times ... \times N_k$-lattice, on which the function y is represented by $N_1...N_k$ functions $y_i(t) = y(t,\vec{x}_i)$ of one variable only.

As I discussed in the previous section, the partial derivatives of y can be approximated by finite differences to a desired order of accuracy. The finite differences are just linear combinations of the functions y_i, and so the right hand side of 197 can be written as

$$F(y(t,\vec{x}_i),\partial_1 y(t,\vec{x}_i),...) = F(y_i(t),A_i\vec{y}(t),...) \equiv \tilde{F}_i(\vec{y}(t)), \qquad (198)$$

where A_i is the matrix operator for the partial derivative at the point $\vec{x}_i$. The partial differential equation can therefore be expressed as

$$\frac{\partial y_i}{\partial t} = \tilde{F}_i(\vec{y}(t)). \qquad (199)$$

The result is a system of coupled ordinary differential equations, which can be solved utilizing the method of one's choosing. Note also that the method of lines generalizes to systems of partial differential equations.

The freedom to use any method for solving the system of ordinary differential equations is the main advantage of the method of lines. In the simulations performed in this thesis, I will always utilize the Runge-Kutta (4,5) -method packaged in the Matlab ode45-algorithm [53]. As the details of the ODE-solver are by design not necessary for using the method of lines, I will not discuss them here.

However, there are some disadvantages to the method as well. The most prominent of these is that the method is difficult to generalize to less symmetric domains, which cannot be expressed as a k-dimensional rectangle. This weakness is shared by most other methods relying on finite differences as well.

I will now turn to the example of an one-dimensional wave equation. Consider the equation

$$\frac{\partial^2 y}{\partial t^2} = c^2 \frac{\partial^2 y}{\partial x^2}, \tag{200}$$

where $x \in [0,1]$ over the time $t \in [0,10]$ and $c \in \mathcal{R}$. I discretize then the spatial domain into N grid points $x_1,...,x_N$ and denote $u_i = y(t,x_i)$. As most ODE-solvers are only applicable to first order differential equations, I also set $u_{N+i} = \dot{y}(t,x_i)$. The wave equation on the lattice becomes the system of equations

$$\partial_t u_i = u_{N+i} \tag{201}$$

$$\partial_t u_{N+i} = c^2 \frac{\partial^2 u_i}{\partial x^2}. \tag{202}$$

For the sake of clarity, I choose the simple second order finite difference for the spatial derivative. Plugging this in results in

$$\partial_t u_i = u_{N+i} \tag{203}$$

$$\partial_t u_{N+i} = \frac{c^2}{h^2}(u_{i+1} - 2u_i + u_{i-1}), \tag{204}$$

with the boundary points determined by the chosen boundary conditions. Adopting periodic boundary conditions results in

$$\partial_t u_{N+1} = \frac{c^2}{h^2}(u_N - 2u_1 + u_2) \tag{205}$$

and the other boundary is handled analogously. The solution to this system of equations can be found with any ODE-solver.

For this example, I choose $c = 1$ and the sinusoidal initial conditions

$$y(0,x) = \sin(2\pi x) \tag{206}$$

$$\dot{y}(0,x) = 2\pi\cos(2\pi x). \tag{207}$$

A plot of the solutions to the wave equation using the method of lines and $N = 32$ is presented in figure 3a along with the analytic solution

$$y_a(t,x) = \sin\left(2\pi(x+t)\right). \tag{208}$$

The error of the method can be estimated with the L^1-norm defined as

$$E_N = \int_0^1 dx \int_0^1 dt |y_a(t,x) - y_N(t,x)|, \tag{209}$$

where y_N is the numerical solution with the grid size N. The errors for solutions with various N can be found in figure 3b, and they show a clear convergence towards the correct solution as the grid spacing decreases.

7.3 Relaxation

In contrast to the hyperbolic evolution equations[8], the constraint equations necessary for solving the initial conditions are elliptic partial differential equations. As the solutions are determined by boundary conditions instead of initial values, the method of lines cannot be be used to find the solution. Because of this, I will utilize the method of relaxation [51].

Relaxation is a method for solving elliptic partial differential equations involving the Laplace operator. Instead of giving a general treatment for the method, it is most illustrative to give an example straight away. Consider the three-dimensional Poisson equation

$$\nabla^2 u = f, \tag{210}$$

where $f = f(\vec{x})$ is a given function. I discretize the the domain with a cubic lattice

---

[8] The ADM-equations can be classified as weakly hyperbolic partial differential equations, and the BSSN-equations are strongly hyperbolic [18].

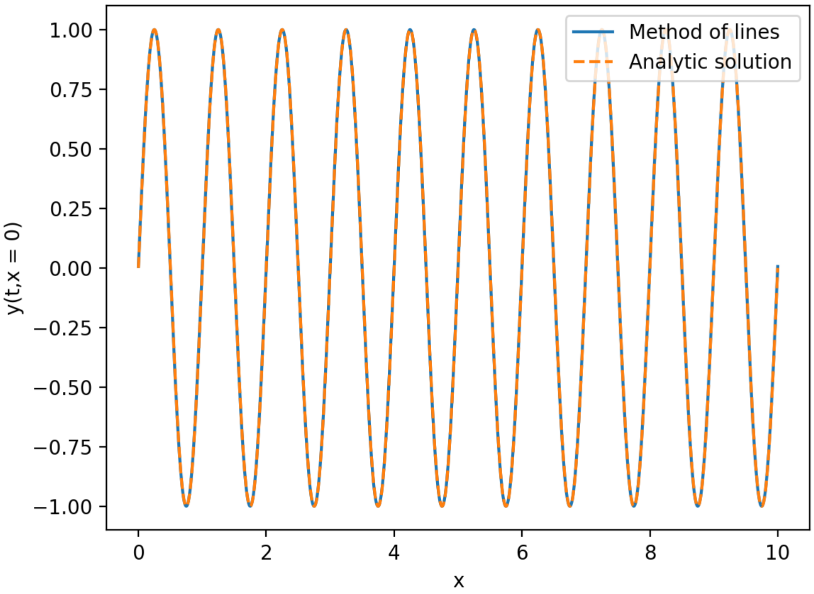

(a)

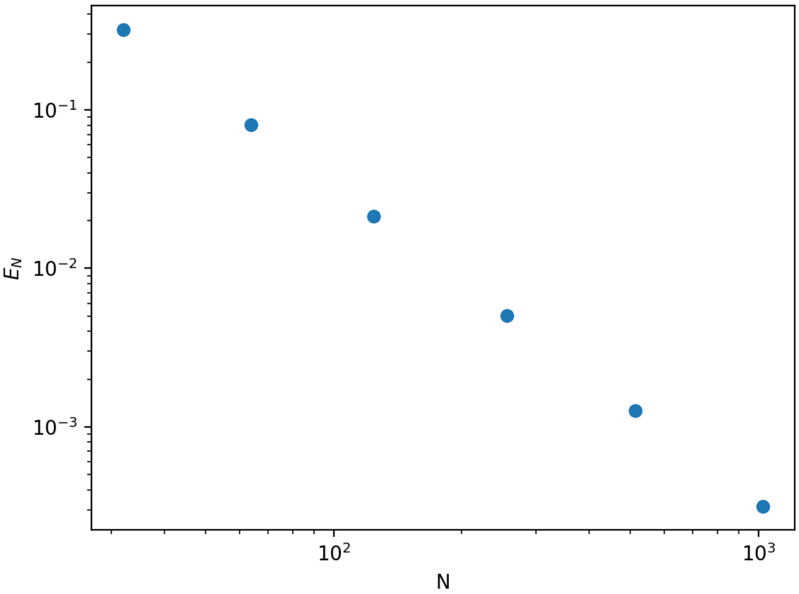

(b)

Figure 3. (a) The method of lines -solution to the wave equation $y(t,x)$ at the point $x = 0$ as a function of time along with the analytic solution (dashed). The grid spacing used was $N = 32$. (b) The error E_N calculated for the method of lines -solutions for the wave equations with different N.

and adopt the notation from section 7.1, that is $u(ih,jh,kh) \equiv u_{ijk}$. For clarity, I will use the second order finite difference for the second derivatives, which leaves the equation as

$$\frac{1}{h^2}\left(-6u_{ijk} + u_{i+1jk} + u_{i-1jk} + u_{ij+1k} + u_{ij-1k} + u_{ijk-1} + u_{ijk-1}\right) = f_{ijk}. \tag{211}$$

Note that boundary points should be handled separately according to the boundary conditions. The value u_{ijk} can be solved as

$$u_{ijk} = \frac{1}{6}\left(u_{i+1jk} + u_{i-1jk} + u_{ij+1k} + u_{ij-1k} + u_{ijk-1} + u_{ijk-1} - h^2 f_{ijk}\right). \tag{212}$$

The solution to the Poisson equation is now found by iterating equation 212 starting from some initial configuration [51]. The convergence of the solution for equation 144 with the filament initial conditions is depicted in figure 4.

The same procedure works for other equations involving the Laplace operator as well, the only modification being extra terms in equation 212. The method can be used even for equations nonlinear in u, although the equivalent of equation 212 cannot necessarily be solved explicitly [54]. In that case, it is common to use a small number of iterations with Newton's method to obtain an approximate solution for u_{ijk} [54]. However, these methods will not be necessary in this thesis.

There are many different schemes for how to perform the iteration. I will adopt the Jacobi iteration

$$u_{ijk}^{N+1} = F_{ijk}(...,u_{i-1jk}^{N},u_{ijk}^{N},u_{i+1jk}^{N},...), \tag{213}$$

where F_{ijk} is the right hand side of the equivalent for equation 212 [51]. The main advantage to the Jacobi iteration is that the right hand side of equation 213 only depends on the values of u at the previous state of iteration, which makes the process easy to vectorize.

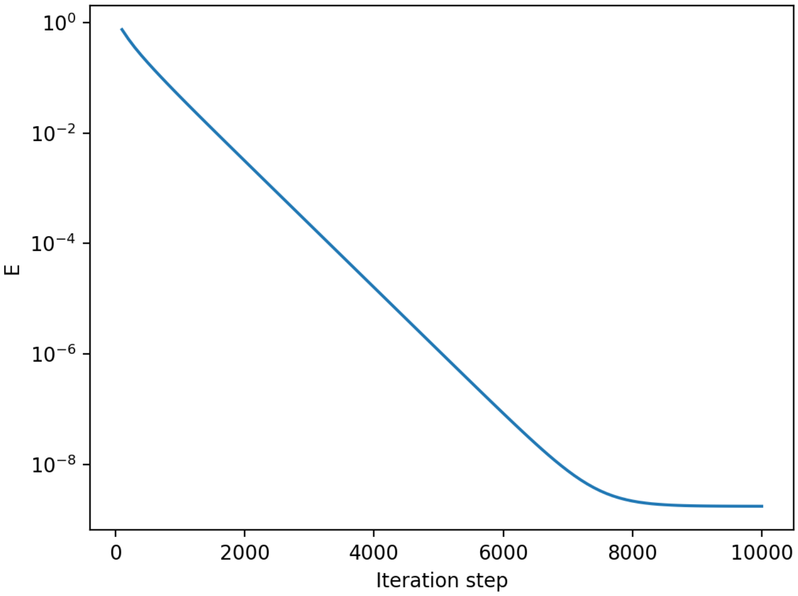

Figure 4. The error $E = \max(|\nabla^2\psi_1 - \bar{f}|)$ for the approximate solutions to the Poisson equation $\nabla^2\psi_1 = \bar{f}$ as a function of relaxation iteration step. Derivatives were approximated with second order finite differences and $\bar{f}$ was chosen according to the filament initial conditions described in section 5.

7.4 Implementation

Here, I will details some of the practical concerns involved with the project. As I stated in the introduction, the goal in this thesis is to implement a numerical simulation of a spacetime using the ADM-formalism and then analyze the behavior of the geodesics in the resulting metric. Even though there are concerns about the stability of the ADM-equations, I will leave the implementation of the BSSN-equations for future research in order to manage the scope of this thesis.

The implementation of the simulations I performed has three main steps:

1. Solve the initial conditions to first order in δ_0 from equation 144 using relaxation. This step can be omitted for the sinusoidal initial conditions, as the Poisson equation can be solved analytically.

2. Starting from the initial conditions, solve the ADM-equations (equations 83 - 85) using the method of lines. As the state vector of the system of differential equations is very large, the progress should be saved to disk periodically in order to free memory.

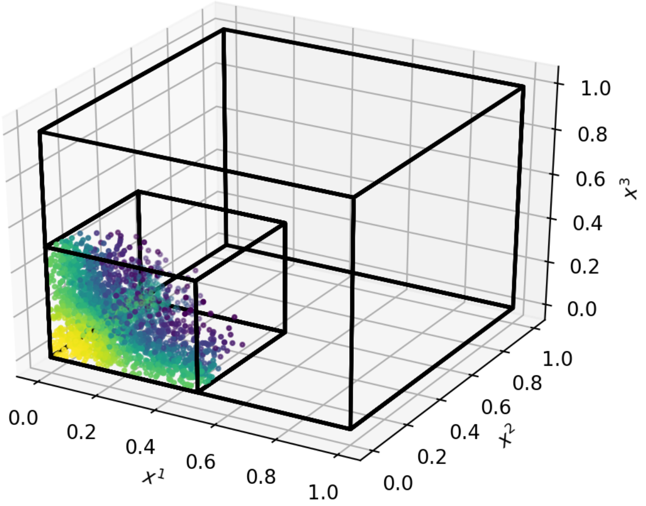

Figure 5. A future solver for the filament initial conditions would only need to simulate one eight of the lattice box due to the reflection symmetries of the problem.

3. Using the saved solution to the ADM-equations as the metric, integrate the geodesic equations (equations 182 and 183) numerically backwards in time for a set of incoming momenta. Calculate the measure of distance, in this case the redshift, along the geodesics and assume that the geodesics are perceived as straight lines to determine the observed pattern of density perturbations.

All the code for this thesis was written in Matlab. The code was intended to be able to run on a consumer laptop, although the runs detailed in the next section were calculated using the Oberon- and Puck-clusters which belong to University of Jyväskylä.

The main limitations to this numerical implementation were the computation time and the available memory. Of these two the computation time was the more constraining one, a full ADM-simulation requiring approximately three days of running time on the cluster with a $50 \times 50 \times 50$ -grid. The system of equations which arises from discretizing the ADM-equations is heavily coupled, and as such major improvements are difficult to achieve using parallelization.

The random-access memory (RAM) available serves as an upper limit to the size of the computational grid on current hardware. In addition to containing the state vector itself, implementing the ADM-equations efficiently required tabulating the finite differences required in calculating the right-hand side of equation 199 on each timestep. One gigabyte of required RAM for the code is reached with an approximately $256 \times 256 \times 256$-grid, with the requirement increasing as N^3. Thus, it is hard to increase the grid size beyond this on our current hardware even if the computational time is increased considerably.

However, a future implementation of the ADM- or BSSN-equations could improve the resolution by a factor of two by utilizing the symmetries of the filament model. As the filament initial conditions have reflection symmetry with respect to the three planes $x^1 = 1/2$, $x^2 = 1/2$ and $x^3 = 1/2$, it is only necessary to simulate one eighth of the lattice box with the proper boundary conditions. This is depicted in figure 5. The solution for the rest of the box could be obtained for analysis by symmetrically extending the solution.

Table 1. The initial condition parameters for each ADM-simulation in this thesis. The different initial condition types are described in section 5.2 and δ_0 is the amplitude parameter of the initial perturbations. The initial time t_{init} was assumed to correspond to the CMB, and the side of the computation box is always $L = 1$ in code units. The corresponding comoving length scale was calculated as detailed in section 5.3.

Run	Initial conditions	δ_0	t_{init}	Comoving length scale
A	Sinusoidal	10^{-5}	1/6	$\sim$ 540 Mpc
B	Sinusoidal	10^{-3}	1/6	$\sim$ 540 Mpc
C	Filament	10^{-3}	1/6	$\sim$ 540 Mpc
D	Filament	10^{-3}	1	$\sim$ 90 Mpc

8 Preliminary results and discussion

In this section, I will discuss the results from both the ADM- and the light propagation simulations. The results presented here are preliminary, and the main question I will address is whether our chosen methods are viable. As such, the results will not correspond to physically realistic situations and will instead serve to highlight different aspects of the simulation. In particular, the density perturbations discussed here are larger than those expected in the actual large scale structure in order to test the nonlinear behaviour of our simulations. I will first focus on the results of the ADM-simulation for the two different initial conditions detailed in section 5. After this, I will move to the light propagation results for the numerical spacetimes obtained from the ADM-equations.

8.1 Sinusoidal initial conditions

The first set of two simulations have the sinusoidal initial conditions as described in section 5.2. Both simulations were run on a $N \times N \times N$-grid, with $N = 50$. The length of the side of the lattice box was set $L = 1$ for simplicity, and the initial time was chosen to be $t_{init} = 1/6$ in code units. As I discussed in section 5.3, I assume that the initial time corresponds to the CMB. With this assumption the choice of t_{init} results in the comoving length scale of 540 Mpc.

As I mentioned in section 5.2, I will choose the initial scale factor $a_{init} = 1$. Since the initial conditions correspond to redshift $z_{CMB} \approx 1100$, the scale factor at the present day should be $a_0 \approx 1100$. I will always plot the results of the simulations with respect to the FLRW-redshift

$$(1+\bar{z})^{-1} := \frac{a(t)}{a_0} = \frac{a(t)}{1100}, \tag{214}$$

where $a(t)$ is the background scale factor as a function of time. However, note that due to the inhomogeneities, $\bar{z}$ is not the actual redshift measured by an observer at the present day. Runs A and B were both set to range from $a = 1$ to $a = 1000$, or equivalently from $\bar{z} = 1099$ until $\bar{z} = 0.1$.

The first of the two simulations had the initial density perturbation amplitude $\delta_0 = 10^{-5}$, and it serves mainly as a comparison with the linear perturbation theory results. Linear perturbation theory predicts that the density perturbations grow approximately linearly with the scale factor in a matter dominated universe [41]. The initial amplitude of the second simulation was $\delta_0 = 10^{-3}$ to ensure that the simulation reaches the nonlinear regime before its end. I will denote these simulations run A and run B respectively. The parameters of the runs can be found in table 1.

The behaviour of the different simulations is the clearest to see by following the the density perturbation at an arbitrarily chosen point. The evolution of the density perturbations are depicted in figure 6 alongside the linear perturbation theory results calculated using equation 20. As expected, the simulation with the small initial perturbation follows closely the linear evolution. However, a close-up of the solution reveals a small oscillation about the analytical result. In contrast, the evolution in run B deviates from the linear result at $\delta \sim 0.1$ as the nonlinear terms grow relevant. At $\bar{z} \approx 0.33$ the timestep chosen by the ode45-algorithm decreases to zero and the simulation terminates.

Estimating the numerical error of the simulations is difficult, as the analytical solutions are not available for comparison outside the limit of small perturbation. As the constraint equations should be zero on each timeslice, I will settle for monitoring the violation of the Hamiltonian constraint. Following [26], I define the normalized

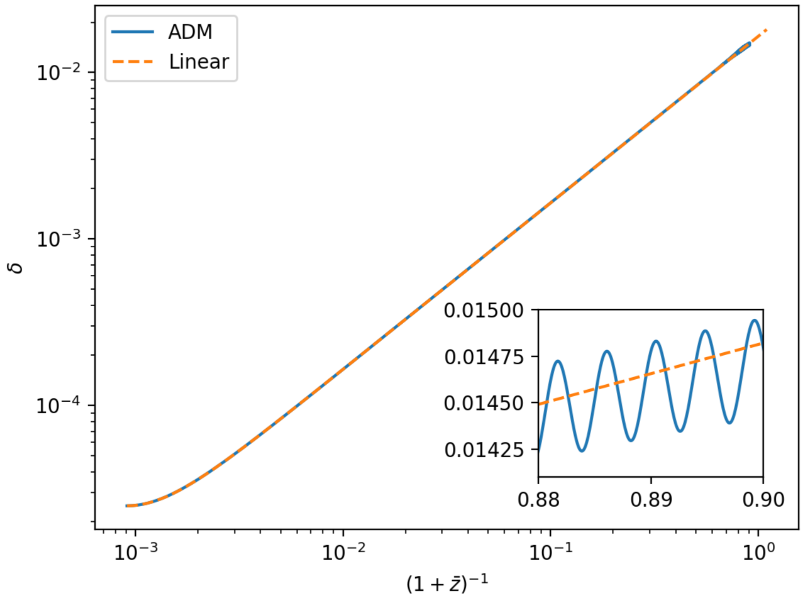

(a) Run A

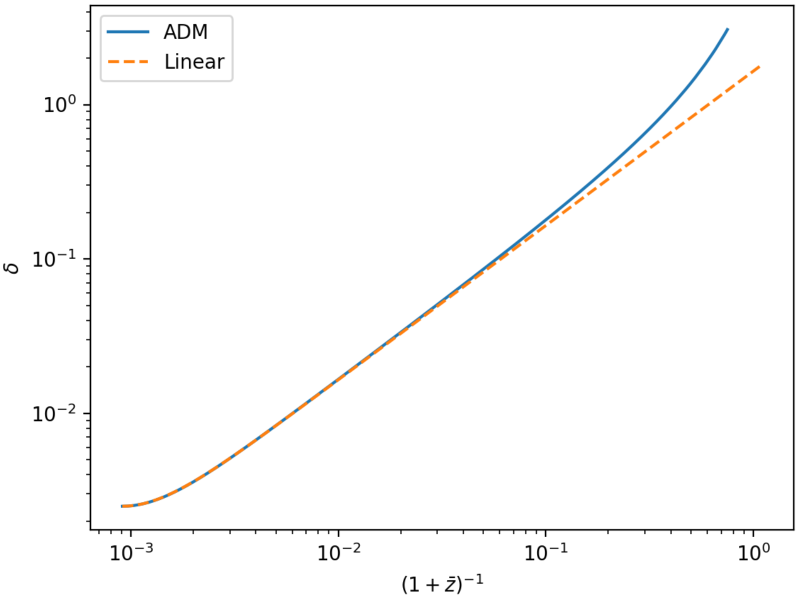

(b) Run B

Figure 6. The evolution of the relative density perturbation δ at the comoving point $(x^1,x^2,x^3) = (0.3,0.16,0.36)$ as a function of the FLRW-redshift $\bar{z}$ for runs A and B. The corresponding results from linear perturbation theory (dashed) are also plotted for comparison. There is no visible oscillation in the results of run B and the simulation terminates at $\bar{z} = 0.33$.

violation of the Hamiltonian constraint E_{HC} as the L^1-norm

$$E_{HC} := \frac{1}{N^3}\sum_{\vec{x}} |R + K^2 - K_{ij}K^{ij} - 16\pi\rho|/\mathcal{N} \tag{215}$$

$$\mathcal{N} := \frac{1}{N^3}\sum_{\vec{x}} \sqrt{R^2 + K^4 + (K_{ij}K^{ij})^2 + (16\pi\rho)^2}, \tag{216}$$

where the sums range over each point on a timeslice.

The errors for the two runs can be found in figure 7. Both cases show similar overall behaviour: The initial errors are small, and they differ by approximately three orders of magnitude. An initial difference by two orders of magnitude or more is to be expected as the initial conditions were solved to a linear approximation. The error decreases for the first few timesteps but then quickly grows rapidly. However, after a period of rapid, noisy fluctuations, the error stabilises and decreases to values smaller than the initial error. The violation of the constraint equation eventually starts to grow again but never reaches the order of unity. The oscillation apparent with the smaller initial perturbation can be seen in the errors of both simulations in the last portion of the simulation. The two simulations differ at the end of the simulation, as the end of simulation B is marked by the error suddenly blowing up.

The overall small scale of E_{HC} increases the confidence in the results. In particular, the fact that the error decreases for a significant portion of the runs suggests that the error present in the initial conditions smooths itself out somewhat. The error starts increasing again at $\bar{z} \approx 4.5$ and $\bar{z} \approx 1.8$ for runs A and B respectively. In particular, this happens later for the larger density contrast and as such it is unlikely that the increase in E_{HC} happens as a result of the nonlinear terms.

A possible source of the initial jump in error are the extrinsic curvature terms in the Hamiltonian constraint. The initial conditions were chosen so that they cancel exactly with the background part of the density term. This is no longer the case after a few timesteps, and if the error in δK_{ij} grows much faster than the error in the metric and the density perturbation, this growth could produce the simulation results.

As opposed to the smaller initial perturbation, the evolution of the larger perturbation differs considerably from the linear perturbation theory. As such, it warrants further attention. While visualizing entire tensor fields is cumbersome, it is useful to consider the evolution of the relative density perturbation δ and the determinant of the spatial metric γ. The spatial volume element is given by the square root $\sqrt{|\gamma|}$,

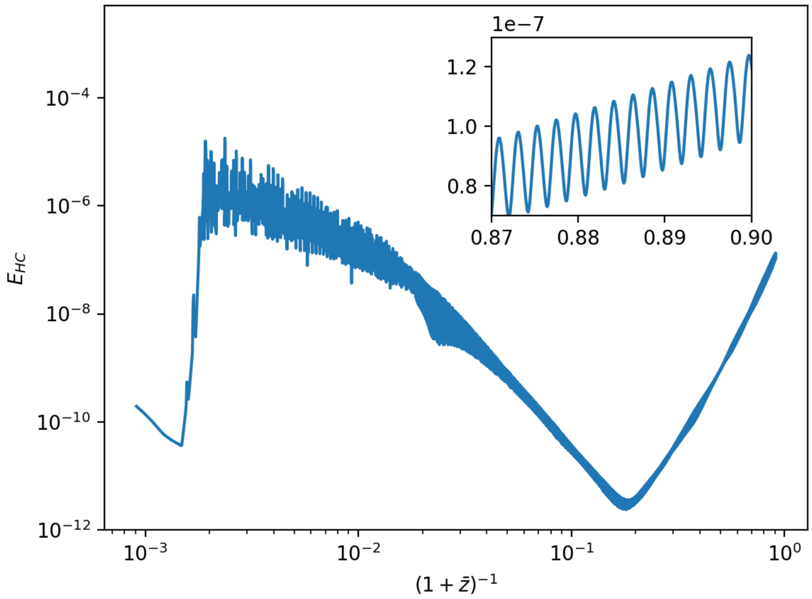

(a) Run A

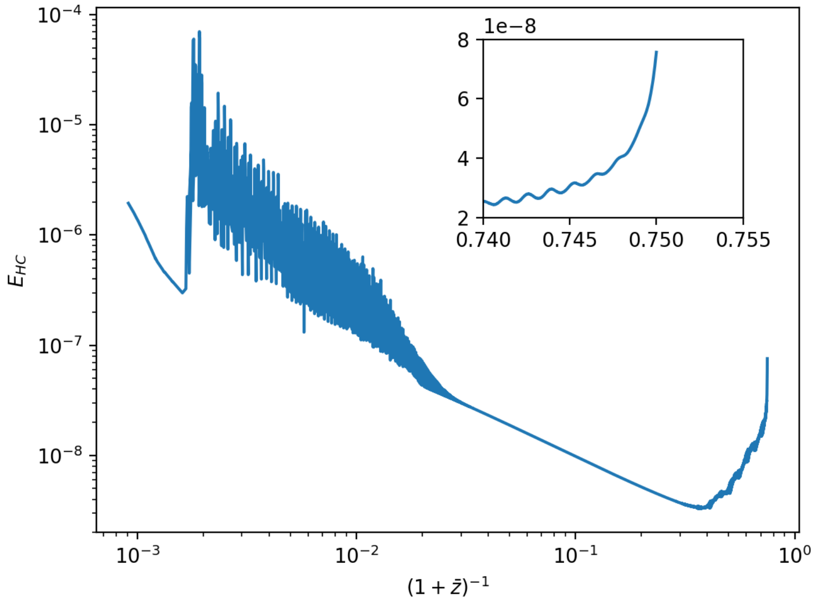

(b) Run B

Figure 7. The evolution of the violation of the Hamiltonian constraint E_{HC} as a function of FLRW-redshift $\bar{z}$ for runs A and B.

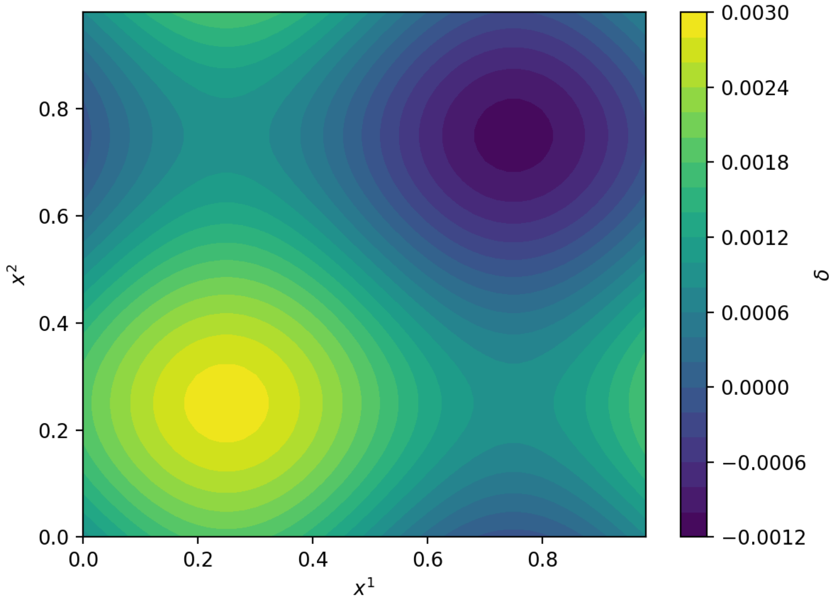

(a) Initial density contrast

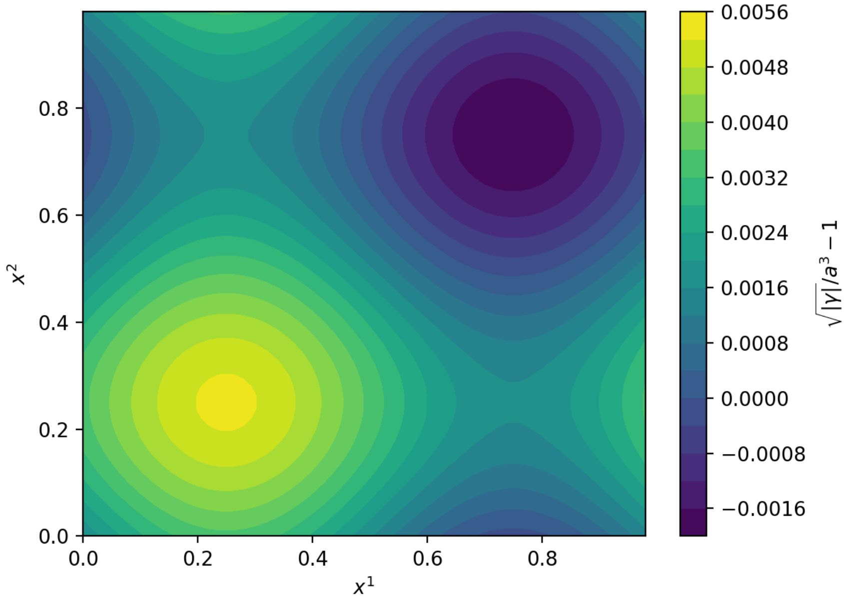

(b) Initial volume element

Figure 8. The relative density contrast δ and the normalized deviation of the volume element $\sqrt{|\gamma|}/a^3 - 1$ on the spatial slice $x^3 = 0.2$ at the initial time $\bar{z} = 1099$ for run B. The initial conditions for run A are identical up to a constant factor. The distributions are shown in the comoving coordinates and in the code units.

and it is useful to define the average scale factor a_{avg} as

$$a_{avg}^3 = \int d^3x \sqrt{|\gamma|}. \tag{217}$$

Note that the average scale factor for the flat FLRW-universe is just a.

Figures 8a and 8b show the initial conditions for δ and $\sqrt{|\gamma|}/a^3$ respectively in run B and the first two panels of figure 9 depicts the evolution of the volume element immediately afterwards. At the initial time, both the volume element and the density perturbation have a sinusoidal deviation from the homogeneous case, with the peaks and the valleys of the two perturbations overlapping. However, the volume element perturbation moves rapidly to an opposite configuration after the simulation begins.

This development happens entirely between two timeslices saved by our simulation. Thus, the possibility that the sudden change is of a numerical origin should not be discounted at this point. A simulation of the early evolution with a smaller time resolution would be warranted to study this.

Disregarding possible numerical issues for now, the behaviour is likely the results of the simplified initial conditions. At the initial time, I required that the trace K is a constant. Since the extrinsic curvature is the time derivative of the spatial metric, K is roughly proportional to the direction-averaged expansion rate. However, since gravity is attractive, an overdense area should expand slower than the average. In order to retain the constant expansion rate, the initial conditions have to introduce a larger initial volume element to compensate for the overdensity. A similar process applies for the underdensities as well.

This evolution suggests that the chosen initial conditions do not match the physical reality. The rapid change in the form of the volume element perturbation happens as the time evolution corrects for the unstable initial configuration. This development can also be connected to the suddenly increasing error in the initial timesteps. The change of the spatial metric is rapid, and so the extrinsic curvature, along with its error, has to be large. This explanation cannot be taken as a certainty, as the large increase in error happens somewhat before the change occurs at $\bar{z} \approx 240$. However, it is possible that the error builds up before the change due to the unstable physical configuration and the change occurs when the system hits a tipping point. I will discuss this further in the context of the subsequent runs. Once the volume element has settled to a more stable form, the evolution proceeds more slowly, and

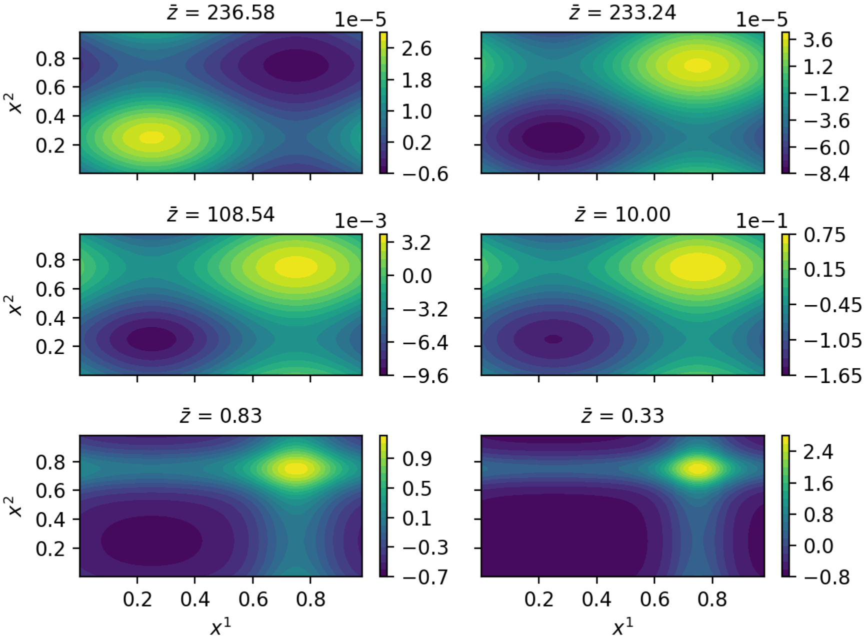

Figure 9. The evolution of the normalized deviation of the volume element $\sqrt{|\gamma|}/a^3 - 1$ on the spatial slice $x^3 = 0.2$ for different timeslices in run B. The distributions are presented in the comoving coordinates and in the code units.

the large error vanishes. The initial stages of the simulation suggest that the resulting metric late in the time evolution is relatively insensitive to the exact initial conditions for the spatial metric and the extrinsic curvature.

After the initial developments, the evolution of the metric and the density perturbations is slow and gradual. The density perturbation and the volume element at the end of the simulation, but before the error blows up, can be found in figures 10a and 10b. The shape of the density perturbation does not change dramatically over the course of the simulation. In the comoving coordinates, the overdensities expand somewhat, although their fraction of the physical volume naturally decreases due to the changes in the volume element. The overdensities are surrounded by a web of underdensities, and the end density contrast between the two extremes is $(1 + \delta_{max})/(1 + \delta_{min}) \approx 16$. Note that the results presented here appear visually different from [24] due to a different gauge choice.

The late evolution of the volume element is very similar to the density perturbation, although the decrease of the comoving volume of the underdensities is more pronounced. The volume element develops a relatively sharp peak in the deepest part of the underdensities. Despite the large maximum of the volume element size, a

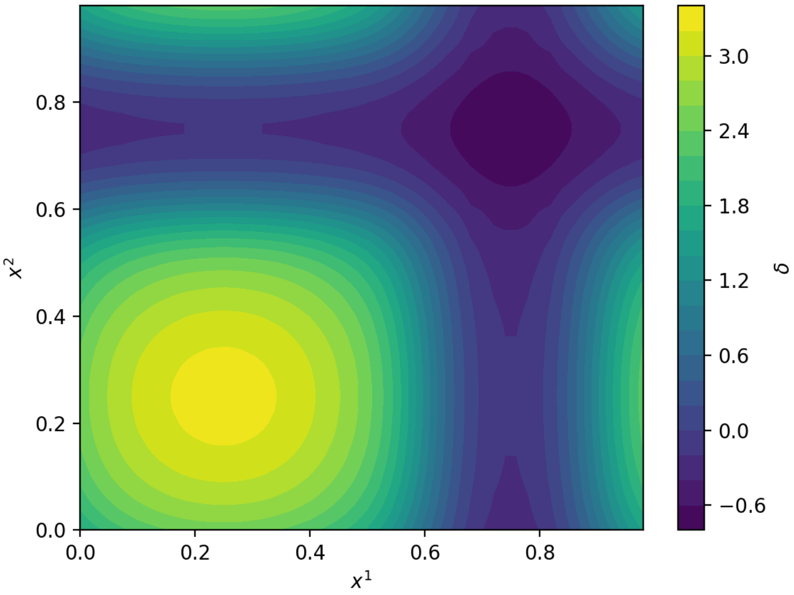

(a) Final density contrast

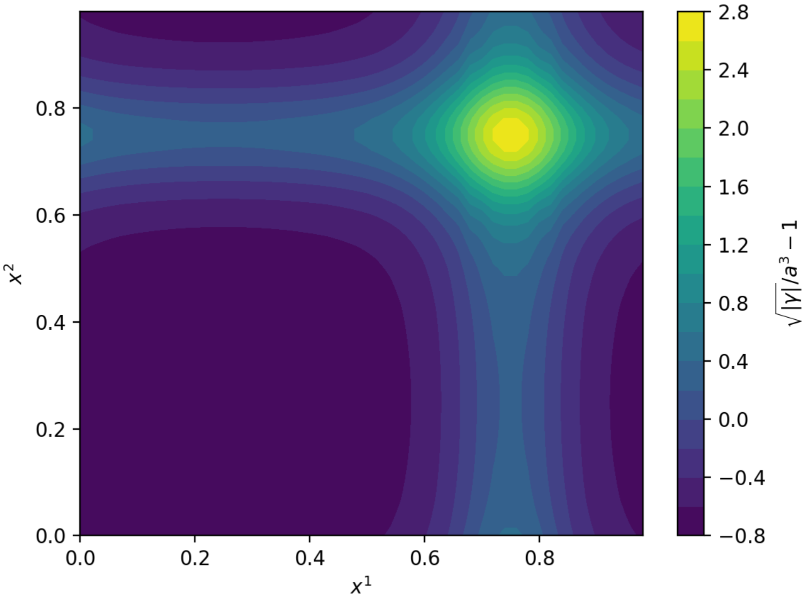

(b) Final volume element

Figure 10. The relative density contrast δ and the normalized deviation of the volume element $\sqrt{|\gamma|}/a^3 - 1$ on the spatial slice $x^3 = 0.2$ in the end of run B at $\bar{z} = 0.33$. The distributions are shown in the comoving coordinates and in the code units.

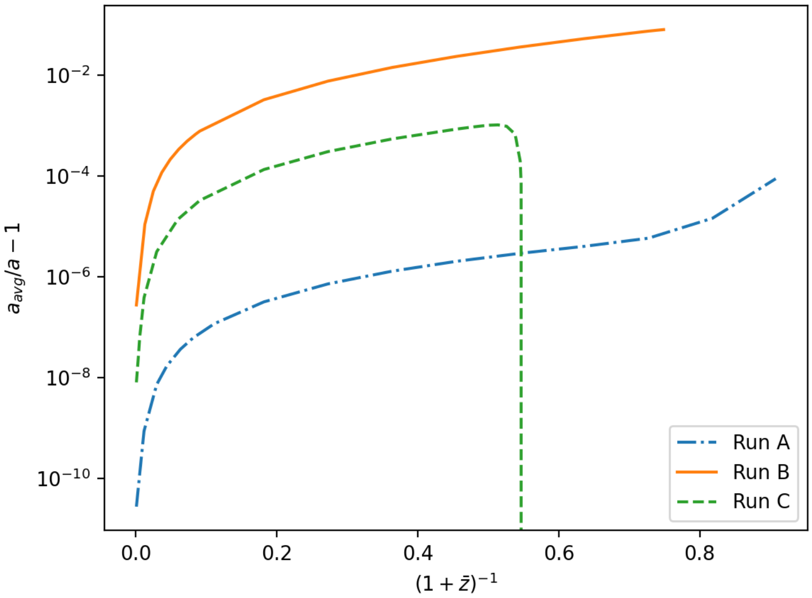

Figure 11. The relative difference of the average scale factor a_{avg} to the FLRW-scale factor a as a function of the FLRW-redshift $\bar{z}$ in runs A, B and C. The average scale factor in run C drops below the FLRW-value before the simulation crashes due to large oscillations in the solution.

large portion of the volume of the underdensities is still located directly between the overdensities, where the volume expands approximately at the same rate as in the homogeneous FLRW-universe.

The overall expansion of the sinusoidal universe is still faster than in a corresponding FLRW-universe, as can be seen from figure 11. At the end of run B, the difference in volumes is approximately 7%, although this result naturally depends heavily on the chosen initial density perturbation. The final density contrast in run B is larger than the contrast expected on the large scales of our own universe [55], and as such the overall expansion rate is likely an overestimate as well.

As I noted above, the simulation with the large initial perturbation terminates at approximately $\bar{z} \approx 0.33$. One possible explanation for this is the instability of the ADM-equations. The ADM-instability can manifest itself as an uncontrollable oscillation in the solution [18, 19]. The oscillations present in the latter portions of the error plot suggest that the ASM-instability is developing. Moreover, at the very end of the simulation, the downward slopes of the oscillation keep turning up, and the error blows up when the slopes become level.

The ADM instability is not the only possible explanation. The resolution of the computational grid use was 0.02 units of length, and at the end of the simulation, the width of the peak in the volume element approaches this scale. The simulation could then become unstable simply due to the limits of the resolution. This scenario could be either confirmed or ruled out by performing the same simulation with a smaller resolution and seeing if this would affect the point where the simulation ends.

8.2 Filament initial conditions

The last two runs I performed used the cubic filament initial density perturbation defined in section 5.2. I used again a $N \times N \times N$-grid with $N = 50$ and the length of the side of the grid was set $L = 1$ in code units. The first of the runs used the same initial time $t_{init} = 1/6$ as the sinusoidal runs, which sets the comoving length scale as 540 Mpc. However, I chose the initial time for the latter run as $t_{init} = 1$ so that the comoving length scale is approximately 90 Mpc. In both simulations, the width parameter of the filaments was $\sigma = 0.15$ in order to ensure that the grid can resolve the filament, while the initial amplitude of the density perturbation was set $\delta_0 = 10^{-3}$. I will denote these simulations run C and run D respectively, and summaries of their parameters are found in table 1.

I solved the initial configuration for the spatial metric to first order in δ_0 from equation 144 using second order relaxation. The convergence for the initial conditions in run C is presented in 4. The initial perturbations for the density and the volume element for run C are presented in figure 12a and the first panel of figure 14a. The corresponding figures for run D differ only by a multiplicative constant.

The behaviour of run C is very similar to run B. As is shown in figure 13a, the error E_{HC} has a similar evolution as before, with the error sharply increasing at the beginning and then dropping gradually until it reaches a minimum value. Afterwards, the error begins to build up at $\bar{z} \approx 2.7$ until it blows up and the simulation terminates at $\bar{z} \approx 0.80$. The increase in error in the latter part of the run is somewhat faster than in run B. As with run B, the configuration of the volume element inverses sharply at the beginning of the run. The shift is somewhat slower than in run B, and the volume element flowing from the filaments to the void can be seen in figure 14a. The change coincides with the initial jump in E_{HC}, which lends credibility to the idea that the jump is a result of the initial conditions. The subsequent evolution of the volume element and the density contrast are very gradual, although the volume

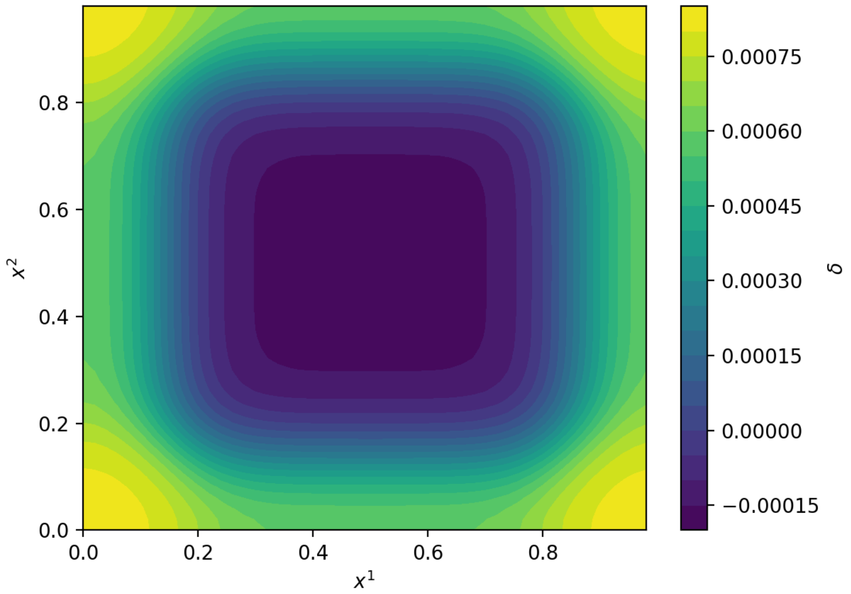

(a) $\bar{z} = 1099$

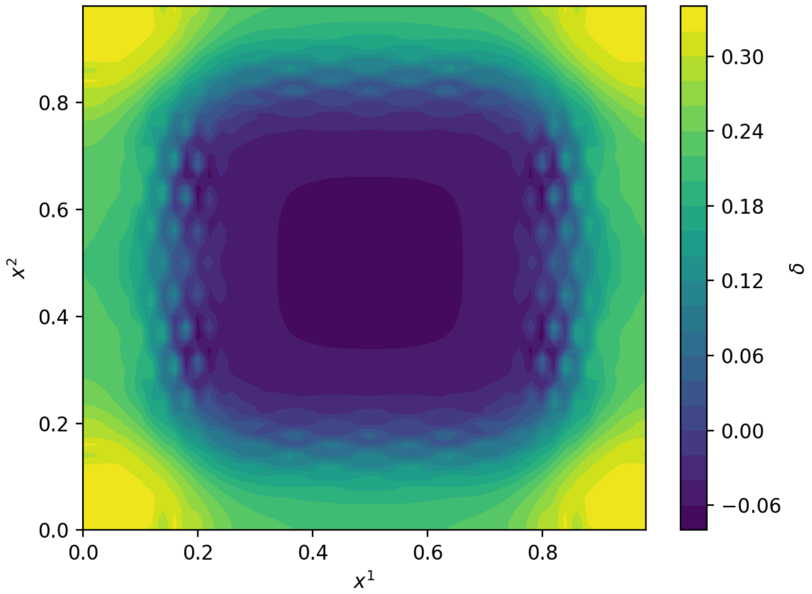

(b) $\bar{z} = 0.83$

Figure 12. The relative density contrast δ on the spatial slice $x^3 = 0$ at the beginning and the end of run C. The simulation crashed at $\bar{z} = 0.80$. The density configuration is depicted with respect to the comoving coordinates and in the code units.

element develops visible oscillations right before the simulation terminates. As one can see in figure 12b, the same oscillations are present in the density contrast.

As run C terminates earlier than run B, its end density contrast is far smaller. This gives further evidence that the increasing density contrast and the nonlinear terms are not the main reason for the simulation ending. However, the difference in the rate of expansion is not only due to the end time. As can be seen from figure 11, the average expansion in run C is two orders of magnitude smaller than in run B at comparable times. This is in spite of the similar amplitudes of initial density contrast. Thus, it appears that the noticeable increase in the average expansion rate found in many inhomogeneous models [15] is not present in our filament model.

Run D differs considerably from the others. As was the case with the other runs, run D was set to span from $\bar{z} = 1099$ until $\bar{z} = 0.1$. However, the behaviour of run D was immediately less stable than that of the others. The timesteps chosen by the ode45-routine were from the start of the simulation shorter than in the previous runs, resulting in a slower progress of the simulation. In the end, I terminated the simulation manually at $\bar{z} \approx 26$ due to E_{HC} increasing exponentially.

The error during run D is depicted in figure 13b and its behaviour has some similarities to runs A, B and C. The initial violation of the Hamiltonian constraint is small, and the initial error is, in fact, smaller for run D than for run B. As before, there is a large increase in error early on in the simulation, and the error begins to decrease afterwards. This change again coincides with a shift in the configuration of the volume element, which can be seen in figure 14b. However, instead of stabilising the error starts to increase again at $\bar{z} \approx 110$ and grows rapidly afterwards. The run was terminated when the error became larger than the scale of the relative density perturbation.

The configuration of the volume element is visually constant until $\bar{z} \approx 43$, at which point the volume element starts to exhibit a visible oscillation. The amplitude of the oscillation grows alongside the error and eventually smears out the entire filament structure. Figure 15 depicts a closeup of the oscillation at $\bar{z} = 33.4$. Notably, the wavelength of the oscillation is roughly the same as the resolution of the computational grid.

The most likely explanations for the failure of the simulation are the same as for the termination of runs B and C. The instability of the ADM-formalism is the most likely scenario. In this case, the trigger for the instability appears to be the change

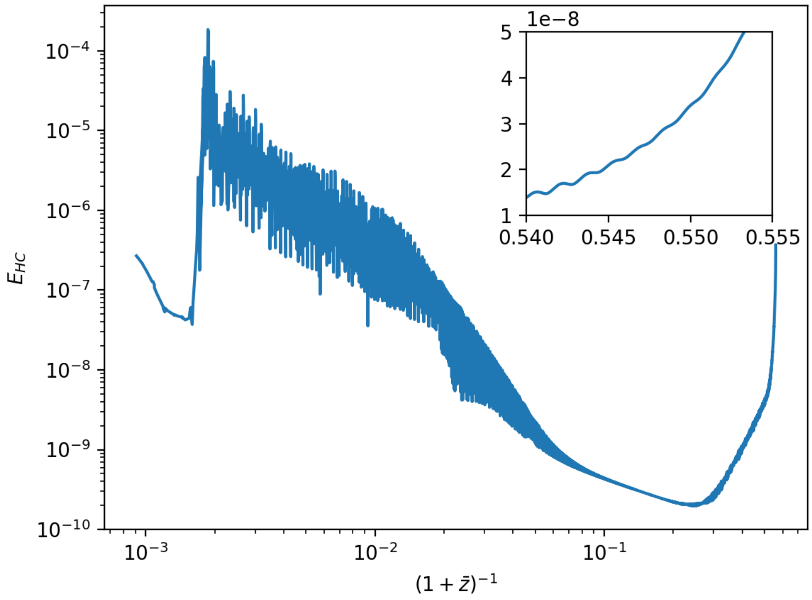

(a) Run C

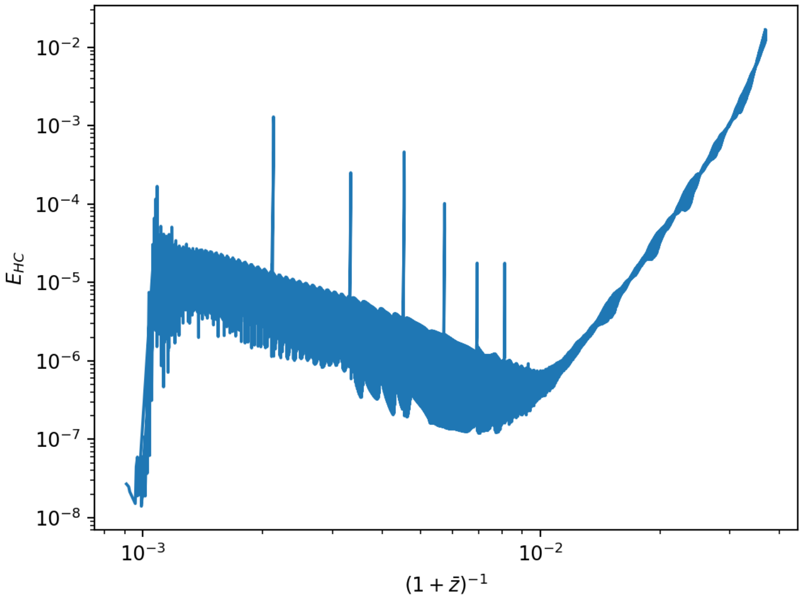

(b) Run D

Figure 13. The evolution of the violation of the Hamiltonian constraint E_{HC} in runs C and D as a function of the FLRW-redshift $\bar{z}$. The timestep of run C approaches zero at $\bar{z} = 0.8$, while run D was terminated manually at $\bar{z} = 26$. The spikes in figure (b) result from individual tentative timesteps of the ode45-routine and should be disregarded.

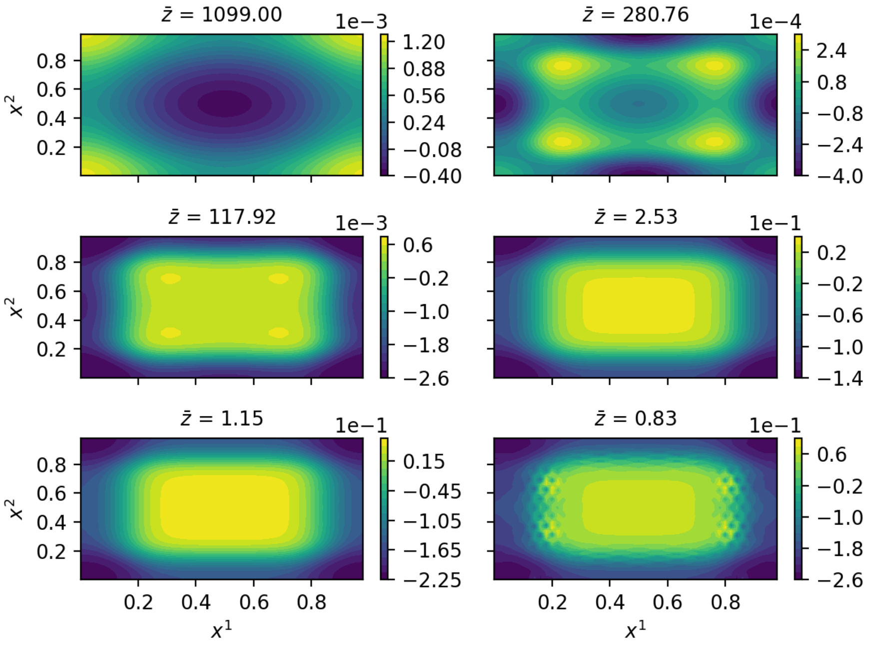

(a) Run C

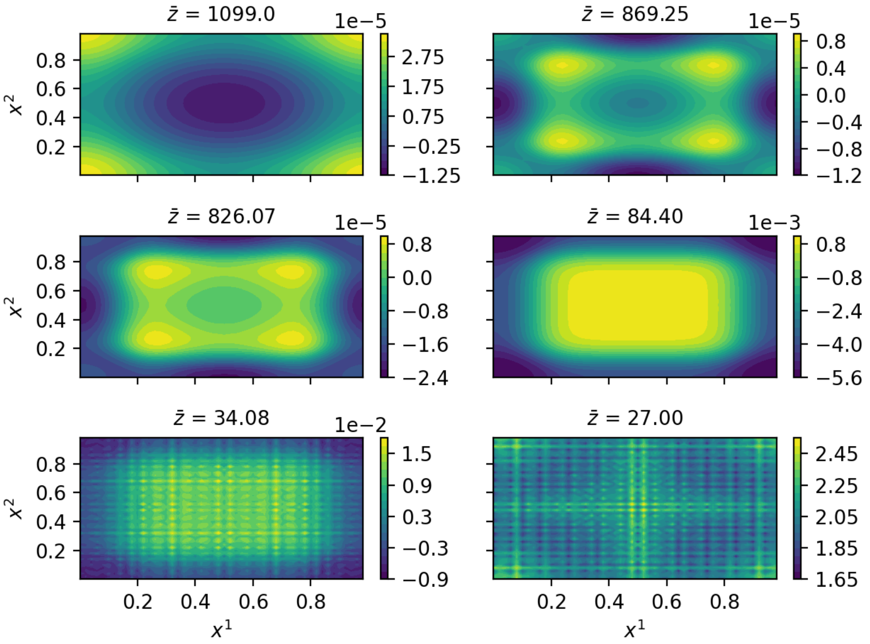

(b) Run D

Figure 14. The evolution of the normalized deviation of the volume element $\sqrt{|\gamma|}/a^3 - 1$ on the spatial slice $x^3 = 0$ in runs C and D. Run D was manually terminated at $\bar{z} = 26$. The figures are plotted in comoving coordinates and in the code units.

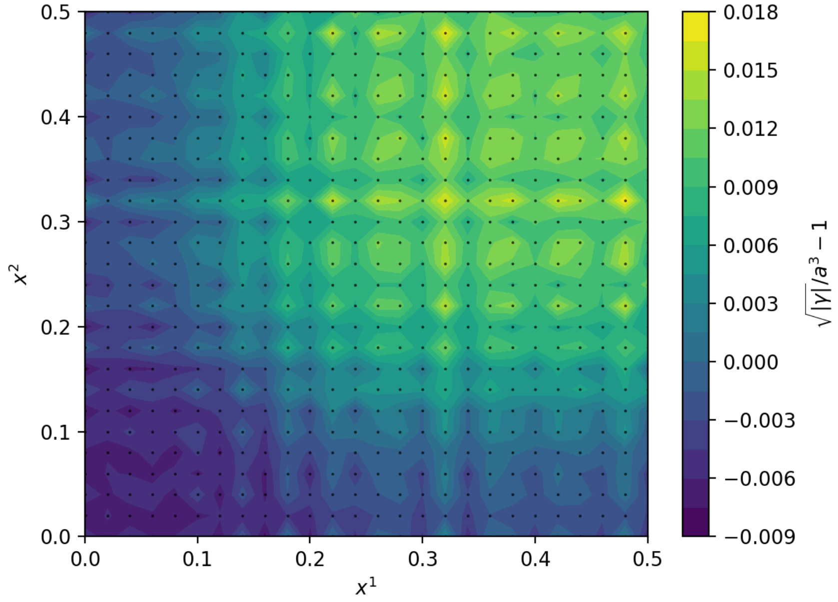

Figure 15. A closeup of the normalized volume element $\sqrt{|\gamma|}/a^3 - 1$ on the spatial slice $x^3 = 0$ at $\bar{z} = 33.4$ in run D. The dots indicate the locations of the grid points and the heatmap is constructed using interpolation. The figure uses comoving coordinates and the code units.

of the scale of the structure. This is not entirely surprising. Due to the change in scale, information travels between different portions of the structure faster, which could explain the drastic difference from the previous runs.

A possible scenario for the developing instability goes as follows: The state of the system develops oscillations along the run, perhaps from numerical inaccuracies or the initial conditions themselves. As the simulation time goes on, the causally connected regions grow, eventually letting the oscillations evolve and terminate the run. It is also worth noting that oscillations were visually present in the solution of run A and could be seen in the errors of all other runs. It is then possible that a similar instability is already developing in the other runs as well, although it didn't grow enough to cause issues early on in the run due to the difference in scale.

As with the end of run B, the lack of resolution could also be at fault. The structures present at the beginning of the run D were somewhat smaller than in the sinusoidal case, which could impact the stability of the early parts of the run. However, as can be seen from figure 15, in the latter part of run D, both the central void and the filaments were large enough to be resolved by the grid. Moreover, the scale of the filaments compared with the resolution is not changed from run C. Therefore, the resolution by itself appears less likely to be at fault.

8.3 Light propagation simulations

As a last part of this thesis, I calculated the behaviour of light trajectories in the numerical spacetimes. Despite the issues with the solutions, I performed the analysis with the results of runs B and C. The light was propagated backwards in time from a chosen end point using equations 182 and 183, and the measured redshift[9] along the rays was obtained from equation 185. The geodesic equations were solved using the Matlab ode45-routine, and I used an interpolation of the ADM-results as the background spacetime. Outside the unit box, I assumed that the spacetime continues periodically.

The first set of 200 light rays have their end point at origin of run B. The incoming momenta were picked in the $x^3 = 0$ -plane at equally spaced angles. The portion of the trajectory from $\bar{z} = 0.33$ until $\bar{z} = 0.83$ for every other ray is depicted in figure 16. As expected, the trajectories show clear gravitational lensing towards the overdensities. Also, in the comoving coordinates, the rays propagate noticeably slower in the voids than in the denser regions due to the difference in the physical volume.

However, the trajectories in the comoving coordinates themselves are not observable. Rather, the measurements observe rays of light from all directions and the distance to an object is determined by using measures of distance such as redshift, luminosity or angular size. The latter two were left out of the scope of this thesis, but the redshift measured by the observer is simple to obtain by using the solutions to the geodesic equation.

The two-dimensional density variation in the $x^3 = 0$ -plane observed in the spacetime of run B is presented in figures 17a and 17b. The observed pattern at $\bar{z} = 0.33$ was determined for two different observer locations, the outskirts of one of the overdensities and in the middle of one of the voids. The patterns were calculated by tracing backwards the incoming light rays arriving at 200 equally spaced angles in the $x^3 = 0$ -plane and assigning the redshift measured by the observer as the

---

[9] Note that this observed redshift is separate from the FLRW-redshift $\bar{z}$ used as a time parameter. The former is the actual redshift measured by an observer at a past point in the inhomogeneous spacetime, while the latter is simply a time parameter defined using the homogeneous background solution.

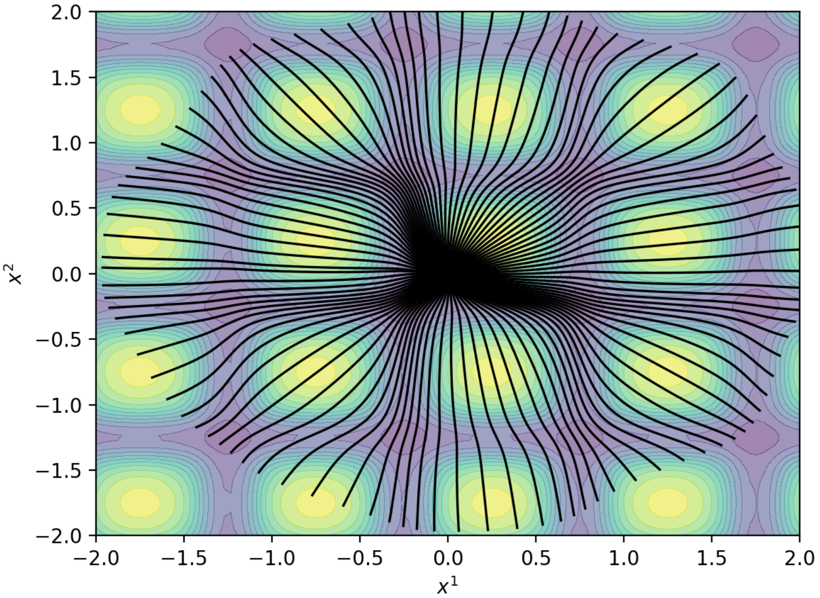

Figure 16. The trajectories of 100 light rays (black) projected to the $x^3 = 0$ spatial plane in run B. The rays end at the origin at $\bar{z} = 0.33$ with no momentum in the x^3-direction. The light was propagated backwards in time until $\bar{z} = 0.83$ and the trajectories are superimposed on the contours of energy density at $\bar{z} = 0.33$. The figure is presented in the comoving coordinates and in code the units.

radial coordinate. Between the rays I used cubic interpolation. I also performed an equivalent calculation for the results of run C with an observer located at $\bar{z} = 0.83$. The observed density perturbations can be found in figures 18a and 18b for observers in the crossing of filaments and in a void respectively.

While a more quantitative analysis and comparisons with measurements will have to wait for further research, there are some general observations to be made. First of all, the angular size of nearby overdensities is magnified compared to their physical size due to gravitational lensing. Similarly, light rays are deflected away from the deepest parts of the voids, which underestimates their size. However, due to the difference in the expansion rates between the two, an inverse effect happens in the redshift. As a result, the voids appear in our observations as stretched in the radial direction, whereas the overdensities stretch in the angular one. This effect is particularly visible with the sinusoidal runs due to the large density contrast, although the elongation of the voids can be seen in run C as well.

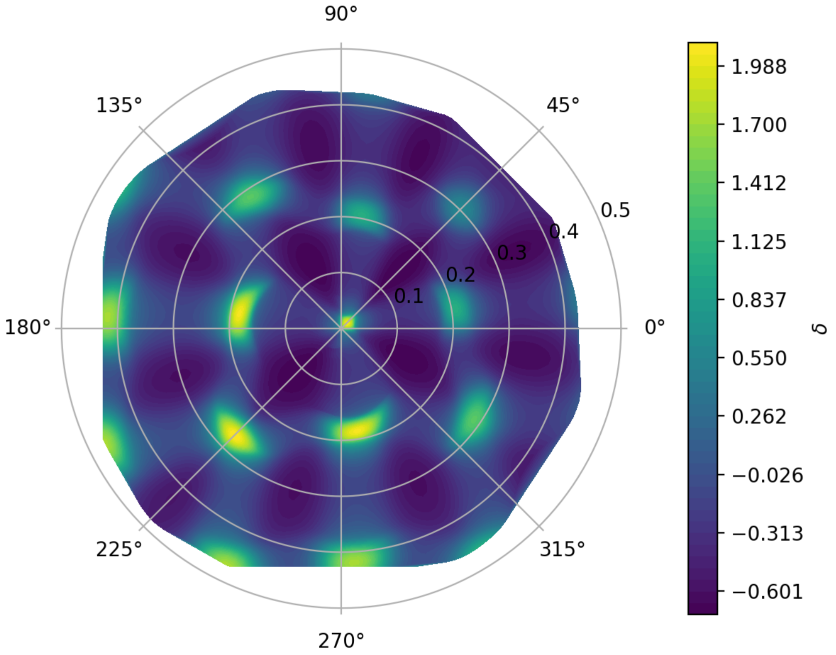

(a) $(x^1_{obs},x^2_{obs}) = (0{,}0)$

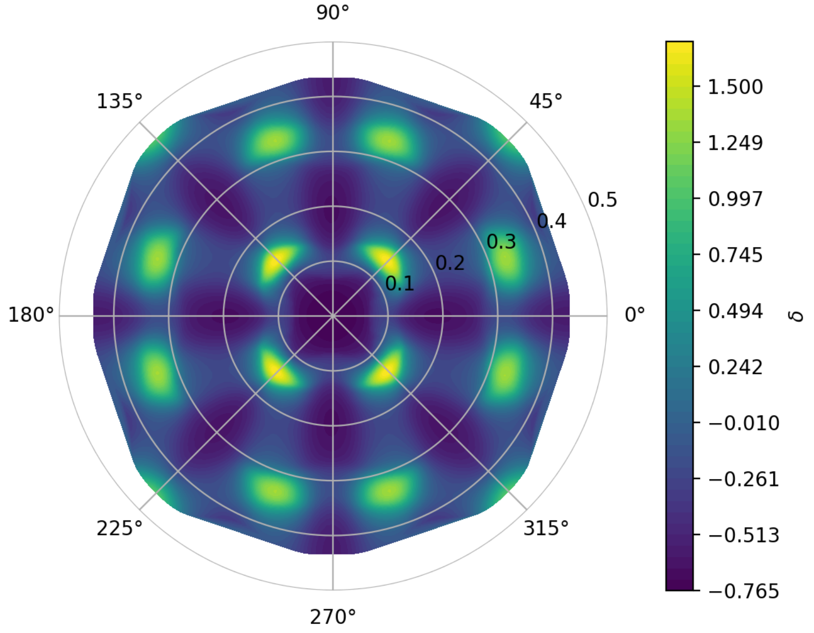

(b) $(x^1_{obs},x^2_{obs}) = (-0.25,-0.25)$

Figure 17. The relative density contrast on the spatial slice $x^3 = 0$ measured by an observer at $(x^1_{obs},x^2_{obs},0)$ and $\bar{z} = 0.33$ in run B. The radial coordinate represents the redshift measured by the observer and the light was propagated back in time until $\bar{z} = 0.83$.

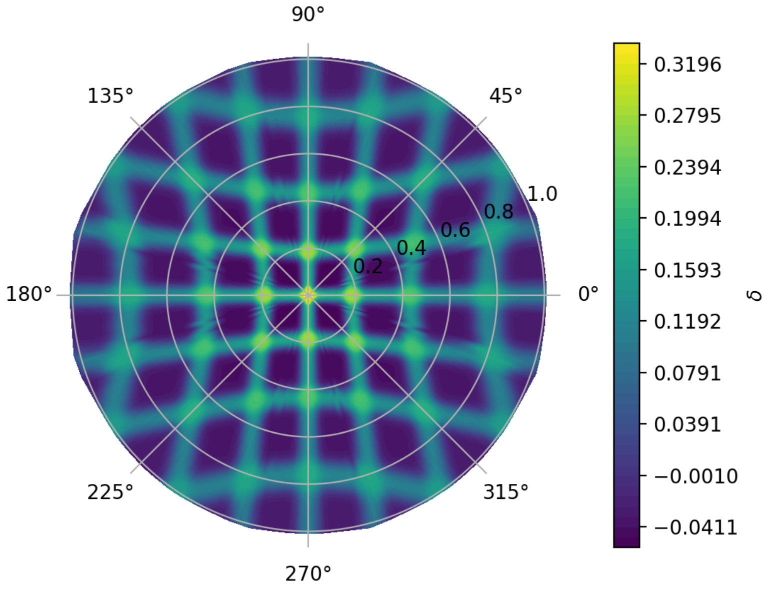

(a) $(x^1_{obs}, x^2_{obs}) = (0{,}0)$

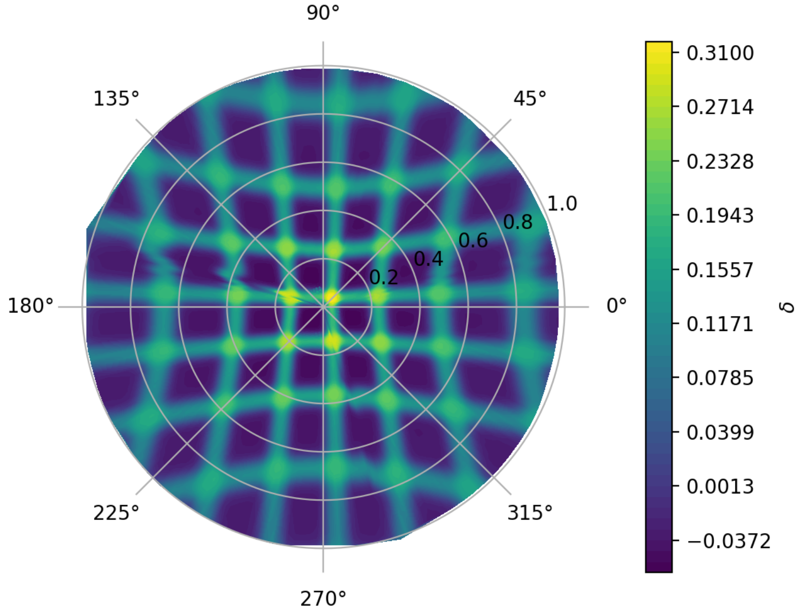

(b) $(x^1_{obs}, x^2_{obs}) = (-0.25, -0.25)$

Figure 18. The relative density contrast on the spatial slice $x^3 = 0$ measured by an observer at $(x^1_{obs}, x^2_{obs}, 0)$ and $\bar{z} = 0.83$ in run C. The radial coordinate represents the redshift measured by the observer and the light was propagated back in time until $\bar{z} = 2.66$. Note that the oscillations present at the late stages of run C create small distortions in both patterns.

The distortion of the light rays could have many effects on measured quantities. For instance, a method for determining the low-redshift expansion rate of the universe is measuring phenomena such as variable stars or supernovae [13]. As the measured events occur disproportionately in the overdense areas, it could be instructive to study whether the gravitational lensing of light in the large-scale structure could bias the measurements in some way.

Another effect visible in the observed patterns is the major asymmetry induced by the location of the observer. This asymmetry is the most pronounced close to the observer, but it is visible even on higher redshifts. In partucular, figure 17a shows how the density perturbations at comparable redshifts appear larger on lower left half of the figure than on the upper right half. However, the asymmetry is heavily dependent on the density contrast, and it is not visible in figure 18b.

9 Summary and outlook

In this thesis, I have presented the ADM- and BSSN-formulations of general relativity in a form ready for numerical implementation. The results are collected in equations 83 - 86 and 128 - 135. I also tested the implementation of the ADM-equations numerically, and to this end I have described two sets of simple initial conditions in section 5. As the metric of the spacetime itself is not an observable quantity, I have also discussed the propagation of light in a general spacetime in section 6 and presented some preliminary results of the simulations in section 8.

The results of the ADM-simulations are mixed. On the one hand, on very large length scales the ADM-formalism produced physically sensible results with a small estimated error for both the sinusoidal and filament initial conditions. This is in the spite of the instability inherent to the ADM-equations, and it might even be interesting to study why the solutions are as stable as they are. On the other hand, at the more physically relevant length scale of 100 Mpc the solutions were immediately unstable and reliable results could not be obtained. There are two main explanations for the numerical issues, the aforementioned ADM-instability and the limits of the resolution. While the results so far suggest the former is the main problem, both of these issues must be addressed before any results can be trusted.

Aside from the numerical issues, the models used in calculating the spacetimes in this thesis have several other main limitations. The assumption that the matter consists of pressureless dust limits the accuracy of the results, as pressure could play a role in matter forming stable halos [56]. Also, the assumption of zero peculiar velocity excludes any possible turbulence. Lastly, in addition to its largest features the actual cosmic web has similar structure on all smaller scales as well. The possible effects of this are very difficult to address numerically due to the finite resolution of any computer simulation.

As opposed to the calculation of the spacetime, the results with the light propagation appear strictly promising. In particular, an interesting aspect of the simulated measurements is the apparent relative size of the voids and the overdensities. While this thesis only discussed this subject on a qualitative basis, a quantitative study of whether the curved trajectories of light bias the measurements could be interesting. However, it must be noted that the density contrast and the overall length scale in our simulated spacetime was far larger than that in the observed large scale structure. Thus, the effects of the curvature seen here are magnified as well.

All in all, there are several avenues for further research. A major focus should be on finding stable solutions on smaller length scales. Resolution as a source of instability could be either confirmed or ruled out by performing simulations with larger grid sizes and comparing the lengths of the simulations. While a naive implementation of this would run into issues with memory and computational time limitations, the resolution could be improved by a factor of two by fully utilising the symmetries of the lattice as described in section 7.4. In principle, many of these problems could also be solved by using an adaptive grid, although implementing one would require a considerable amount of work.

Regardless of whether an increase in resolution solves the pressing issues, it appears necessary to move on to the BSSN-formalism. The simulations run here seem to lie close to the limits of the ADM-formulation. Thus, the same results should be obtained with the BSSN-equations before they can be relied on. Should moving to BSSN-equations fail to solve the stability issues, the solution for the spacetime could be calculated using the Einstein toolkit [25]. The applicability of the full BSSN-formalism even with small grid sizes has already been demonstrated by simulations such as [24].

Even though the light propagation simulations presented here appear to function without major issues, it is still missing a large component as well, namely the calculation of the luminosity- and angular distances. Calculating these as a function of redshift along different rays of light would allow comparisons with the supernova distance measurements [57, 58]. The angular distance in a general spacetime has been calculated in [9, 10], which could serve as the starting point for a numerical implementation.

References

[1] J. K. Yadav, J. S. Bagla, and N. Khandai. “Fractal dimension as a measure of the scale of homogeneity”. In: *Monthly Notices of the Royal Astronomical Society* (Apr. 2010), no–no. ISSN: 1365-2966. DOI: `10.1111/j.1365-2966.2010.16612.x`. URL: `http://dx.doi.org/10.1111/j.1365-2966.2010.16612.x`.

[2] S. Nadathur. “Seeing patterns in noise: gigaparsec-scale “structures” that do not violate homogeneity”. In: *Monthly Notices of the Royal Astronomical Society* 434.1 (July 2013), pp. 398–406. ISSN: 1365-2966. DOI: `10.1093/mnras/stt1028`. URL: `http://dx.doi.org/10.1093/mnras/stt1028`.

[3] I. Horvath, J. Hakkila, and Z. Bagoly. *The largest structure of the Universe, defined by Gamma-Ray Bursts*. 2013. arXiv: `1311.1104 [astro-ph.CO]`.

[4] V. F. Mukhanov. *Physical foundations of cosmology*. Cambridge, UK New York: Cambridge University Press, 2005. ISBN: 0-521-56398-4.

[5] P. J. E. Peebles. *The large-scale structure of the universe*. Princeton, N.J: Princeton University Press, 1980. ISBN: 978-0691082400.

[6] D. Gorbunov. *Introduction to the theory of the early universe : cosmological perturbations and inflationary theory*. Singapore Hackensack, N.J: World Scientific, 2011. ISBN: 978-981-4322-22-5.

[7] T. Buchert. “On Average Properties of Inhomogeneous Fluids in General Relativity: Dust Cosmologies”. In: *General Relativity and Gravitation* 32.1 (Jan. 2000), pp. 105–125. ISSN: 1572-9532. DOI: `10.1023/a:1001800617177`. URL: `http://dx.doi.org/10.1023/A:1001800617177`.

[8] T. Buchert and S. Räsänen. “Backreaction in Late-Time Cosmology”. In: *Annual Review of Nuclear and Particle Science* 62.1 (Nov. 2012), pp. 57–79. ISSN: 1545-4134. DOI: `10.1146/annurev.nucl.012809.104435`. URL: `http://dx.doi.org/10.1146/annurev.nucl.012809.104435`.

[9] M. Lavinto. “Light Propagation and Observations in Inhomogeneous Cosmological Models”. PhD thesis. Helsinki: Helsinki Institute of Physics, University of Helsinki, 2015. URL: `http://urn.fi/URN:ISBN:978-951-51-1262-0`.

[10] E. Poisson. *A Relativist’s Toolkit: The Mathematics of Black-Hole Mechanics.* Cambridge University Press, 2004. DOI: `10.1017/CBO9780511606601`.

[11] N. Aghanim et al. “Planck 2018 results”. In: *Astronomy and Astrophysics* 641 (Sept. 2020), A6. ISSN: 1432-0746. DOI: `10.1051/0004-6361/201833910`. URL: `http://dx.doi.org/10.1051/0004-6361/201833910`.

[12] A. G. Riess et al. “Cosmic Distances Calibrated to 1% Precision with Gaia EDR3 Parallaxes and Hubble Space Telescope Photometry of 75 Milky Way Cepheids Confirm Tension with ΛCDM”. In: *The Astrophysical Journal* 908.1 (Feb. 2021), p. L6. ISSN: 2041-8213. DOI: `10.3847/2041-8213/abdbaf`. URL: `http://dx.doi.org/10.3847/2041-8213/abdbaf`.

[13] E. Di Valentino et al. “In the realm of the Hubble tension—a review of solutions *”. In: *Classical and Quantum Gravity* 38.15 (July 2021), p. 153001. ISSN: 1361-6382. DOI: `10.1088/1361-6382/ac086d`. URL: `http://dx.doi.org/10.1088/1361-6382/ac086d`.

[14] S. Castello, M. Högås, and E. Mörtsell. *A Cosmological Underdensity Does Not Solve the Hubble Tension.* 2021. arXiv: `2110.04226 [astro-ph.CO]`.

[15] S. Räsänen. “Accelerated expansion from structure formation”. In: *Journal of Cosmology and Astroparticle Physics* 2006.11 (Nov. 2006), pp. 003–003. ISSN: 1475-7516. DOI: `10.1088/1475-7516/2006/11/003`. URL: `http://dx.doi.org/10.1088/1475-7516/2006/11/003`.

[16] L. Tenhu. “On Explaining the Tension in the Observations of the Hubble Parameter by the wLTB model”. master’s thesis. Jyväskylä: University of Jyväskylä, Department of Physics, 2018. URL: `https://jyx.jyu.fi/handle/123456789/59920` (visited on 10/25/2021).

[17] R. Arnowitt, S. Deser, and C. W. Misner. “Dynamical Structure and Definition of Energy in General Relativity”. In: *Phys. Rev.* 116 (5 Dec. 1959), pp. 1322–1330. DOI: `10.1103/PhysRev.116.1322`. URL: `https://link.aps.org/doi/10.1103/PhysRev.116.1322`.

[18] T. W. Baumgarte and S. L. Shapiro. *Numerical Relativity: Solving Einstein's Equations on the Computer*. Cambridge University Press, 2010.

[19] T. W. Baumgarte and S. L. Shapiro. "Numerical integration of Einstein's field equations". In: *Physical Review D* 59.2 (Dec. 1998). ISSN: 1089-4918. DOI: `10.1103/physrevd.59.024007`. URL: `http://dx.doi.org/10.1103/PhysRevD.59.024007`.

[20] M. Shibata and T. Nakamura. "Evolution of three-dimensional gravitational waves: Harmonic slicing case". In: *Phys. Rev. D* 52 (10 Nov. 1995), pp. 5428–5444. DOI: `10.1103/PhysRevD.52.5428`. URL: `https://link.aps.org/doi/10.1103/PhysRevD.52.5428`.

[21] B. P. Abbott et al. "Observation of Gravitational Waves from a Binary Black Hole Merger". In: *Physical Review Letters* 116.6 (Feb. 2016). ISSN: 1079-7114. DOI: `10.1103/physrevlett.116.061102`. URL: `http://dx.doi.org/10.1103/PhysRevLett.116.061102`.

[22] M. Campanelli et al. "Accurate Evolutions of Orbiting Black-Hole Binaries without Excision". In: *Phys. Rev. Lett.* 96 (11 Mar. 2006), p. 111101. DOI: `10.1103/PhysRevLett.96.111101`. URL: `https://link.aps.org/doi/10.1103/PhysRevLett.96.111101`.

[23] E. Bentivegna and M. Bruni. "Effects of Nonlinear Inhomogeneity on the Cosmic Expansion with Numerical Relativity". In: *Physical Review Letters* 116.25 (June 2016). ISSN: 1079-7114. DOI: `10.1103/physrevlett.116.251302`. URL: `http://dx.doi.org/10.1103/PhysRevLett.116.251302`.

[24] H. J. Macpherson, P. D. Lasky, and D. J. Price. "Inhomogeneous cosmology with numerical relativity". In: *Physical Review D* 95.6 (Mar. 2017). ISSN: 2470-0029. DOI: `10.1103/physrevd.95.064028`. URL: `http://dx.doi.org/10.1103/PhysRevD.95.064028`.

[25] Z. Etienne et al. *The Einstein Toolkit*. Version The "Lorentz" release, ET_2021_05. To find out more, visit http://einsteintoolkit.org. May 2021. DOI: `10.5281/zenodo.4884780`. URL: `https://doi.org/10.5281/zenodo.4884780`.

[26] H. J. Macpherson, D. J. Price, and P. D. Lasky. "Einstein's Universe: Cosmological structure formation in numerical relativity". In: *Physical Review D*

99.6 (Mar. 2019). ISSN: 2470-0029. DOI: `10.1103/physrevd.99.063522`. URL: `http://dx.doi.org/10.1103/PhysRevD.99.063522`.

[27] S. Carroll. *Spacetime and geometry : an introduction to general relativity*. Harlow, Essex: Pearson, 2014. ISBN: 978-1-29202-663-3.

[28] T. Frankel. *The geometry of physics : an introduction*. Cambridge New York: Cambridge University Press, 2012. ISBN: 978-1107602601.

[29] M. S. Longair. *A brief history of cosmology*. Vol. 2. Citeseer, 2004.

[30] E. P. Hubble. "A spiral nebula as a stellar system, Messier 31." In: *Astrophysical Journal* 69 (Mar. 1929), pp. 103–158. DOI: `10.1086/143167`.

[31] A. Friedmann. "Über die Krümmung des Raumes". In: *Zeitschrift fur Physik* 10 (Jan. 1922), pp. 377–386. DOI: `10.1007/BF01332580`.

[32] G. Lemaitre. "Un Univers homogène de masse constante et de rayon croissant rendant compte de la vitesse radiale des nébuleuses extra-galactiques". In: *Annales de la Société Scientifique de Bruxelles* 47 (Jan. 1927), pp. 49–59.

[33] H. P. Robertson. "Kinematics and World-Structure II." In: *The Astrophysical Journal* 83 (Apr. 1936), p. 187. DOI: `10.1086/143716`.

[34] H. P. Robertson. "Kinematics and World-Structure II." In: *The Astrophysical Journal* 83 (Apr. 1936), p. 187. DOI: `10.1086/143716`.

[35] H. P. Robertson. "Kinematics and World-Structure III." In: *The Astrophysical Journal* 83 (May 1936), p. 257. DOI: `10.1086/143726`.

[36] A. G. Walker. "On Milne's theory of world-structure". In: *Proceedings of the London Mathematical Society* 2.1 (1937), pp. 90–127.

[37] E. Hubble. "A relation between distance and radial velocity among extra-galactic nebulae". In: *Proceedings of the National Academy of Sciences* 15.3 (1929), pp. 168–173. ISSN: 0027-8424. DOI: `10.1073/pnas.15.3.168`. eprint: `https://www.pnas.org/content/15/3/168.full.pdf`. URL: `https://www.pnas.org/content/15/3/168`.

[38] A. A. Penzias and R. W. Wilson. "A Measurement of Excess Antenna Temperature at 4080 Mc/s." In: *Astrophysical Journal* 142 (July 1965), pp. 419–421. DOI: `10.1086/148307`.

[39] H. W. Babcock. "The rotation of the Andromeda Nebula". In: *Lick Observatory Bulletin* 498 (Jan. 1939), pp. 41–51. DOI: `10.5479/ADS/bib/1939LicOB.19.41B`.

[40] F. Zwicky. "On the Masses of Nebulae and of Clusters of Nebulae". In: *The Astrophysical Journal* 86 (Oct. 1937), p. 217. DOI: `10.1086/143864`.

[41] E. Kolb and M. Turner. *The early universe.* New York: Westview Press, 1994. ISBN: 978-0201626742.

[42] J. R. Gott III et al. "A Map of the Universe". In: *The Astrophysical Journal* 624.2 (May 2005), pp. 463–484. ISSN: 1538-4357. DOI: `10.1086/428890`. URL: `http://dx.doi.org/10.1086/428890`.

[43] R. B. Tully. "Alignment of Clusters and Galaxies on Scales up to 0.1 C". In: *The Astrophysical Journal* 303 (Apr. 1986), p. 25. DOI: `10.1086/164049`.

[44] S. Perlmutter et al. "Measurements of Ω and Λ from 42 High-Redshift Supernovae". In: *The Astrophysical Journal* 517.2 (June 1999), pp. 565–586. ISSN: 1538-4357. DOI: `10.1086/307221`. URL: `http://dx.doi.org/10.1086/307221`.

[45] A. G. Riess et al. "Observational Evidence from Supernovae for an Accelerating Universe and a Cosmological Constant". In: *The Astronomical Journal* 116.3 (Sept. 1998), pp. 1009–1038. ISSN: 0004-6256. DOI: `10.1086/300499`. URL: `http://dx.doi.org/10.1086/300499`.

[46] V. Springel et al. "Simulations of the formation, evolution and clustering of galaxies and quasars". In: *Nature* 435.7042 (June 2005), pp. 629–636. DOI: `10.1038/nature03597`. arXiv: `astro-ph/0504097 [astro-ph]`.

[47] É. Gourgoulhon. *3+1 formalism in general relativity : bases of numerical relativity.* Berlin New York: Springer, 2012. ISBN: 978-3-642-24524-4.

[48] L. E. Kidder, M. A. Scheel, and S. A. Teukolsky. "Extending the lifetime of 3D black hole computations with a new hyperbolic system of evolution equations". In: *Physical Review D* 64.6 (Aug. 2001). ISSN: 1089-4918. DOI: `10.1103/physrevd.64.064017`. URL: `http://dx.doi.org/10.1103/PhysRevD.64.064017`.

[49] E. Bentivegna. “Solving the Einstein constraints in periodic spaces with a multigrid approach”. In: *Classical and Quantum Gravity* 31.3 (Dec. 2013), p. 035004. ISSN: 1361-6382. DOI: `10.1088/0264-9381/31/3/035004`. URL: `http://dx.doi.org/10.1088/0264-9381/31/3/035004`.

[50] S. A. Hughes et al. “Finding black holes in numerical spacetimes”. In: *Phys. Rev. D* 49 (8 Apr. 1994), pp. 4004–4015. DOI: `10.1103/PhysRevD.49.4004`. URL: `https://link.aps.org/doi/10.1103/PhysRevD.49.4004`.

[51] W. Press et al. *Numerical recipes : the art of scientific computing.* Cambridge, UK New York: Cambridge University Press, 2007. ISBN: 9780521880688.

[52] B. Fornberg. “Generation of finite difference formulas on arbitrarily spaced grids”. In: *Mathematics of computation* 51.184 (1988), pp. 699–706.

[53] J. Dormand and P. Prince. “A family of embedded Runge-Kutta formulae”. In: *Journal of Computational and Applied Mathematics* 6.1 (1980), pp. 19–26. ISSN: 0377-0427. DOI: `https://doi.org/10.1016/0771-050X(80)90013-3`. URL: `https://www.sciencedirect.com/science/article/pii/0771050X80900133`.

[54] M. Vrahatis, G. Magoulas, and V. Plagianakos. “From linear to nonlinear iterative methods”. In: *Applied Numerical Mathematics* 45.1 (2003), pp. 59–77.

[55] R. C. Keenan, A. J. Barger, and L. L. Cowie. “Evidence for a $\sim$ 300 megaparsec scale under-density in the local galaxy distribution”. In: *The Astrophysical Journal* 775.1 (Sept. 2013), p. 62. ISSN: 1538-4357. DOI: `10.1088/0004-637x/775/1/62`. URL: `http://dx.doi.org/10.1088/0004-637X/775/1/62`.

[56] J. Bovy. *Dynamics and Astrophysics of Galaxies.* NJ: Princeton University Press, 2021, (in preparation).

[57] A. G. Riess et al. “Type Ia Supernova Discoveries atz> 1 from theHubble Space Telescope: Evidence for Past Deceleration and Constraints on Dark Energy Evolution”. In: *The Astrophysical Journal* 607.2 (June 2004), pp. 665–687. ISSN: 1538-4357. DOI: `10.1086/383612`. URL: `http://dx.doi.org/10.1086/383612`.

[58] D. M. Scolnic et al. “The Complete Light-curve Sample of Spectroscopically Confirmed SNe Ia from Pan-STARRS1 and Cosmological Constraints from the Combined Pantheon Sample”. In: *The Astrophysical Journal* 859.2, 101 (June 2018), p. 101. DOI: `10.3847/1538-4357/aab9bb`. arXiv: `1710.00845 [astro-ph.CO]`.